Antibacterial and fluorescent clear aligner attachment resin modified with chlorhexidine loaded mesoporous silica nanoparticles and zinc oxide quantum dots

DOI:
10.1016/j.jmbbm.2023.105817

Document Version
Accepted author manuscript

Published in:
Journal of the mechanical behavior of biomedical materials

Antibacterial and fluorescent clear aligner attachment resin modified with chlorhexidine loaded mesoporous silica nanoparticles and zinc oxide quantum dots

Lingyun Cao[a, b, 1], Jiarong Yan[a, b, 1], Ting Luo[a, b], Huiyi Yan[a], Fang Hua[a, c, d, *], Hong He[a, b, *]

[a.] The State Key Laboratory Breeding Base of Basic Science of Stomatology (Hubei-MOST) & Key Laboratory for Oral Biomedical Ministry of Education, School & Hospital of Stomatology, Wuhan University, Wuhan 430079, China

[b.] Department of Orthodontics, School & Hospital of Stomatology, Wuhan University, Wuhan 430079, China

[c.] Center for Orthodontics and Pediatric Dentistry at Optics Valley Branch, School & Hospital of Stomatology, Wuhan University, Wuhan 430000, China

[d.] Division of Dentistry, School of Medical Sciences, Faculty of Biology, Medicine and Health, University of Manchester, Manchester M13 9PL, UK

*** Correspondence**
Assoc. Prof. Fang Hua
Center for Orthodontics and Pediatric Dentistry at Optics Valley Branch
School & Hospital of Stomatology, Wuhan University, Luoyu Road 237, Wuhan 430079, China
Email: huafang@whu.edu.cn

Prof. Hong He
Department of Orthodontics
School & Hospital of Stomatology, Wuhan University, Luoyu Road 237, Wuhan 430079, China
Email: drhehong@whu.edu.cn

[1] Lingyun Cao and Jiarong Yan contributed equally to this work.

https://doi.org/10.1016/j.jmbbm.2023.105817

Abstract

Objectives: To develop an antibacterial and fluorescent clear aligner attachment resin via the incorporation of chlorhexidine loaded pore-expanded mesoporous silica nanoparticles (CHX@pMSN) and amino-silane functionalized zinc oxide quantum dots ($aZnO_{QDs}$), and to evaluate its antibacterial activity, fluorescence capability, esthetic properties, mechanical performance and biocompatibility.

Methods: CHX@pMSN and $aZnO_{QDs}$ were incorporated into the commercial resin composites (Filtek Z350 XT, 3M) at different mass fractions, control group: Filtek; fluorescent attachment resin (FAR): Filtek + 3 wt.% $aZnO_{QDs}$; antibacterial and fluorescent attachment resin (AFAR)-1: Filtek + 3 wt.% $aZnO_{QDs}$ + 1 wt.% CHX@pMSN; AFAR-2: Filtek + 3 wt.% $aZnO_{QDs}$ + 3 wt.% CHX@pMSN; AFAR-3: Filtek + 3 wt.% $aZnO_{QDs}$ + 5 wt.% CHX@pMSN. CHX release, antibacterial activity, fluorescence capability, color change, stain resistance, degree of conversion, depth of cure, polymerization shrinkage, water sorption and solubility, softening in solvent, flexural strength, flexural modulus, shear bond strength, and cytotoxicity were evaluated comprehensively.

Results: CHX could be continuously released from the AFAR groups for up to 30 days. CFU, MTT, lactic acid production, SEM and CLSM evaluation showed AFAR-2 and AFAR-3 could effectively inhibit *S. mutans* biofilm even after 1-month aging. Only AFAR-3 showed clinically perceptible color change and all the experimental groups were not more susceptible to staining. AFAR-1 and AFAR-2 could suppress polymerization shrinkage and enhance the resistance to degradation without compromising other properties, including degree of conversion, water sorption and solubility, flexural strength, flexural modulus, and shear bond strength. Depth of cure of all the four experimental groups was significantly decreased ($p < 0.05$) but still within the ISO standard. CCK-8 assay and live/dead cell staining denied the cytotoxicity of experimental resins. Fluorescence intensity tests showed that FAR and AFAR-2 could emit strong yellowish fluorescence under the excitation of ultraviolet for up to six months.

Conclusions: AFRA-2 possessed long-term antibiofilm activity, strong fluorescence capability and satisfying biocompatibility without compromising esthetic and mechanical properties. This study proposed a new strategy for reducing bacteria accumulation around the attachment, which is also promising in helping orthodontists to remove the attachment thoroughly and precisely.

Keywords: Clear aligner attachment; Zinc oxide quantum dots; Chlorhexidine; Mesoporous silica nanoparticles; Antibacterial activity; Florescence.

1. Introduction

Nowadays, with an increasing demand for esthetics and health, clear aligner treatment has gained great popularity among adult and adolescent patients(Eliades et al., 2020). Compared with fixed orthodontic appliances, clear aligners have many advantages, such as better esthetics, removability, shorter chair-time and fewer visits(Elshazly et al., 2022). Furthermore, patients treated with clear aligners were reported to experience lower levels of pain during their first days of treatment(Cardoso et al., 2020). It is generally believed that clear aligners can facilitate oral hygiene maintenance and thereby reduce enamel demineralization compared to fixed appliances. However, it was found that for the patients treated with clear aligners, the oral microbiome was not significantly improved compared with those treated with fixed appliances(Wang et al., 2019b). During the clear aligner treatment, teeth and gingiva are covered with aligners for more than 22 hours per day, which may promote the formation of the acquired pellicle and biofilms(Xie et al., 2020). It has been reported that patients undergoing clear aligner treatment were more prone to developing shallower but larger white spot lesions (WSLs) than those undergoing fixed orthodontic treatment(Albhaisi et al., 2020).

Clear aligner attachments are small geometries made of tooth-colored materials, necessary for almost every patient undergoing clear aligner treatment. The attachments on enamel surface maximize the contacts between the aligner and the teeth and deliver the orthodontic force to the teeth, which could enhance the aligner retention and facilitate to achieve more efficient tooth movements(Chen et al., 2021; Feinberg et al., 2016; Mantovani et al., 2019). However, the attachments, due to their irregular shapes protruding from the teeth, introduce retention sites on tooth surfaces, encouraging a greater degree of biofilm formation(Eliades et al., 2020; Low et al., 2011). The food and bacteria are more likely to get attached to and accumulated around the attachments. Covering a significant portion of the tooth surface, the attachments might contribute to the difficulties in oral hygiene maintenance and increase the incidence of WSLs.

To reduce visibility, the attachment is highly required for its esthetic properties, especially in the esthetic zone of the front teeth(Feinberg et al., 2016). Thus, the clear aligner attachment should match the tooth color as close as possible. However, unlike

traditional restorative dental resin, the clear aligner attachment resin needs to be removed at the end of the treatment(Eliades et al., 2020). Due to the similar color of the enamel and the attachment resin, it would be very demanding for orthodontists to completely remove the attachments. Inadequate removal of the attachment resin could lead to discoloration and bacteria accumulation, impairing patients' esthetics and health. Excessive removal of the attachment resin could directly result in enamel damages. Therefore, from the aforementioned points above, the development of a novel clear aligner attachment resin, which has strong antibacterial ability and can be distinguished from enamel under certain conditions, would be quite promising.

In recent years, quantum dots (QDs), the highly luminescent nanocrystals, have found extensive applications in medical fields(Gulia and Rita Kakkar, 2013). Among these, much attention has been paid to ZnO quantum dots (ZnO_{QDs}) because of their strong fluorescence capability, unique photodynamic antibacterial ability, and low toxicity(Garcia et al., 2018; Gulia and Rita Kakkar, 2013). Under the ultraviolet excitation, ZnO_{QDs} could emit yellowish fluorescence(Yan et al., 2022a). It was reported that the amino-silane functionalized ZnO_{QDs} ($aZnO_{QDs}$) possessed enhanced water solubility, fluorescence capability and biocompatibility(Zhao et al., 2013). In the field of dentistry, ZnO_{QDs} have been utilized as nanofillers for adhesive resins and have been incorporated into the orthodontic adhesives (Garcia et al., 2016; Garcia et al., 2018; Yan et al., 2022a). Fluorescence capability and antibacterial ability have been successfully gifted, and the mechanical properties of the resins did not compromise(Garcia et al., 2016; Garcia et al., 2018; Yan et al., 2022a). However, the antibacterial property of ZnO remains disputed(Arun et al., 2020; Gulia and Rita Kakkar, 2013). Previous study reported that the ZnO nanoparticles modified composites possessed no peripheral antibacterial effect due to the low solubility of the ZnO nanoparticles(Aydin Sevinc and Hanley, 2010; Tavassoli Hojati et al., 2013). Moreover, the antibacterial effect of the ZnO nanoparticles modified composites may not be long-lasting(Aydin Sevinc and Hanley, 2010; Tavassoli Hojati et al., 2013).

Chlorhexidine (CHX), the "gold standard" for the evaluation of antimicrobial agents, has a wide antibacterial spectrum and low cytotoxicity towards mammalian cells(Yan et al., 2018; Yan et al., 2017). CHX has been widely applied in the dental field such as mouth

rinse, dental coating, and denture wash(Slot et al., 2011). Attempts have been made to realize the antibacterial ability of the dental composites by incorporating CHX into the resins(Anusavice et al., 2006; Yan et al., 2018; Zhang et al., 2014). Nevertheless, simply blending CHX into the resins could lead to CHX aggregation, decreased strength and increased water sorption of the resin, and cause a porous surface after CHX release (Zhang et al., 2014). In the last decades, mesoporous silica nanoparticles (MSN) have emerged as a novel approach as a delivery system for sustained drug release, including antibacterial, anti-inflammatory and anti-cancer agents(Tang et al., 2012; Yan et al., 2017). CHX has also been successfully loaded in MSN (CHX@MSN) to achieve elongated antibacterial activity against oral biofilms(Seneviratne et al., 2014). Recently, CHX-loaded pore-expanded MSN (CHX@pMSN) has been developed and a high amount of drug loading has been achieved(Yan et al., 2018). The CHX@pMSN was further incorporated into dentin adhesive and glass ionomer cement and successfully realized 30 days sustained release of CHX, without affecting their mechanical performance(Yan et al., 2018; Yan et al., 2017).

In this study, we aimed to explore the feasibility of incorporating $aZnO_{QDs}$ and CHX@pMSN into the clear aligner attachment resin to realize fluorescence and long-term antibacterial modifications. Null hypotheses of this research are as follows: the novel clear aligner attachment resin modified with $aZnO_{QDs}$ and CHX@pMSN (1) does not have antibacterial activity, (2) does not have fluorescence capability, (3) does not have appropriate esthetic property, (4) does not have acceptable biocompatibility, and (5) does not have acceptable mechanical performance.

2. Materials and methods

2.1. Synthesis of $aZnO_{QDs}$ and CHX@pMSN

The sol-gel method reported in our previous study was utilized to synthesize $aZnO_{QDs}$ with some modifications(Wang et al., 2012; Yan et al., 2022a). 3.3 g of zinc acetate dihydrate (Sigma, US) was dissolved in 90 mL ethanol and refluxed with stirring for two hours in water baths at 80 ℃. 1.176 g of KOH (Sigma, US) was dissolved in 12 mL ethanol. The KOH solution was then dropped into the zinc acetate solution and vigorously stirred at

the same time for 20 mins to obtain the ZnO_{QDs} suspension. The solution containing 240 μL of 3-aminopropyl triethoxysilane (APTES, Sigma, US) and 1.2 mL of deionized water was slowly dropped into the mixture and vigorously stirred simultaneously. After centrifugation and vacuum dried at room temperature, the $aZnO_{QDs}$ powder was obtained.

The synthesis of pMSN (mobile crystalline material 41 type, MCM-41) and loading of CHX were based on a previously reported technique with some modifications(Yan et al., 2018; Yang et al., 2017). Briefly, 0.5 g of cetyltrimethylammonium bromide (CTAB, Sigma, US) was dissolved in a solution containing 240 mL deionized water and 1.75 mL of 2 mol/L NaOH (Sigma, US). 3.5 mL of 1,3,5-mesitylene (TMB, Sigma, US) was then incorporated as the pore-expanding agent. After vigorously stirring for 4 h at 80 °C, 2.5 mL tetraethyl orthosilicate (TEOS, Sigma, US) was added to the solution and stirred for another 2 h at 80 °C. The sediment was centrifuged, washed with deionized water and ethanol, and oven-dried overnight at 60 °C. Afterward, the product was calcined in a muffle furnace at 550 ℃ in the air for 5 h, and the pMSN was obtained.

1g of CHX diacetate salt hydrate (Sigma, US) and 200 mg of pMSN was dissolved in 20 mL of ethanol. The solution was then sonicated for 30 mins and vigorously stirred for three days at room temperature. The mixture (CHX@pMSN) was centrifuged, washed with ethanol three times, and oven-dried overnight at 60 °C.

2.2. Characterization of $aZnO_{QDs}$ and CHX@pMSN

$aZnO_{QDs}$ were characterized by transmission electron microscope (TEM, JEM-2100, JEOL, Japan), Fourier transform infrared (FT-IR) spectrometer (FTIR5700, Thermo, US), and X-ray diffractometer (XRD, SmartLab SE, Rigaku, Japan). aZn_{QDs} suspension was characterized via fluorescence spectrophotometer (F7000, Hitachi, Japan). Photos of aZn_{QDs} powders were obtained under natural light, ultraviolet light and mixing light (natural light + ultraviolet light).

pMSN and CHX@pMSN were characterized by TEM (JEM-2100, JEOL, Japan), field-emission scanning electron microscope (FESEM, GeminiSEM 500, Zeiss, Germany), and small angle XRD (SmartLab SE, Rigaku, Japan). Elemental mapping was also performed for CHX@pMSN with TEM (JEM-F200, JEOL, Japan). FT-IR spectra (FTIR5700, Thermo,

US) were conducted for CHX powder, pMSN, and CHX@pMSN. Thermogravimetric analysis (STA449F3, NETZSCH, Germany) with a heating rate of 10 ℃/min from room temperature to 1000 ℃was conducted to assess the weight percentage of CHX loading in pMSN. Surface characteristics of pMSN and CHX@pMSN were analyzed by the nitrogen adsorption-desorption isotherm with high throughput surface area and porosity analyzer (TriStar Ⅱ 3020, Micromeritics, US). The Brunauer–Emmett–Teller (BET) and Barrett–Joyner–Halenda (BJH) analyses were employed to calculate the specific surface area, pore volume, and pore diameter distribution.

2.3. Preparation of experimental attachment resin

Commercial composite resin (Filtek Z350XT, 3M ESPE, US) routinely used for clear aligner attachments was utilized as the resin matrix(Chen et al., 2021; Feinberg et al., 2016). CHX@pMSN powders were wet with the silane coupler (Monobond N, Ivoclar Vivadent, UK). $aZnO_{QDs}$ and CHX@pMSN were then manually blended into the resin matrix, followed by mixing in an amalgamator (ProMixTM, Dentsply Caulk, US) in darkness to improve the homogenization of the composite mixture. The caps of 0.5 mL Eppendorf tubes were utilized as the mold for making the resin discs (Ø 6.5 mm, H 1 mm). After being filled into the caps, the resin was light cured (Bluephase Style, Ivoclar-Vivadent Amherst, US) for 30 s and was polished with 800-, 1000-, and 2000-grit SiC sandpapers under running water. According to our preliminary tests, the incorporation of 3 wt.% $aZnO_{QDs}$ could grant composite resin with strong fluorescent ability. Therefore, five groups were set as follows:

- Control Group: Filtek Z350XT
- FAR (Fluorescent Attachment Resin): Filtek Z350XT + 3 wt.% $aZnO_{QDs}$
- AFAR-1 (Antibacterial and Fluorescent Attachment Resin-1): Filtek Z350XT + 3 wt.% $aZnO_{QDs}$ + 1 wt.% CHX@pMSN
- AFAR-2 (Antibacterial and Fluorescent Attachment Resin-2): Filtek Z350XT + 3 wt.% $aZnO_{QDs}$ + 3 wt.% CHX@pMSN
- AFAR-3 (Antibacterial and Fluorescent Attachment Resin-3): Filtek Z350XT + 3 wt.%

$aZnO_{QDs}$ + 5 wt.% CHX@pMSN

2.4. CHX release

For AFAR-1, AFAR-2, and AFAR-3 groups, CHX release was tested with high-performance liquid chromatography (Agilent1100, Palo Alto, US). The height and diameter of the resin discs from each group (n = 3) was measured by a digital micrometer (accurate to 0.01 mm) and the surface area was then calculated. The disks were stored in 5 mL of deionized water in an incubator at 37°C. At each time point (day 1, 3, 7, 10, and 30), 1 mL of the solution was taken and the CHX concentration was measured, and 1 mL of sterile deionized water was then added to maintain the volume of the solution (Yan et al., 2018). The cumulative release of CHX from the three groups at each time point was calculated.

2.5. Antibacterial activities

2.5.1. Specimen preparation

Sixty-three resin disks per group (Ø 6.5 mm, H 1 mm) were prepared for antibacterial activity test, 24 for MTT assay, 18 for lactic acid measurement, 9 for CFU evaluation, 6 for scanning electron microscope (SEM) observation, and 6 for confocal laser scanning microscopy (CLSM) observation. For each test, resin discs were randomly divided into three subgroups, including immediate subgroup, 1-week subgroup, and 1-month (30 days) subgroup, to test the immediate and long-term antibacterial activity of the experimental resins.

For the immediate subgroup, discs were stored overnight at 37 ℃ in artificial saliva (Sigma, US) before being subjected to biofilm cultivation. For the 1-week subgroup and 1-month subgroup, resin discs were further kept in 1 mL of daily replaced artificial saliva for 7 days and 30 days, respectively. Before the biofilm cultivation, discs were disinfected with 75% alcohol and rinsed with sterile phosphate-buffered saline (PBS) thrice.

2.5.2. Biofilm cultivation

Streptococcus mutans (*S. mutans*, UA159), provided by the School of Stomatology, Wuhan University (China), was micro-aerobically (5% CO_2, 1% O_2) incubated at 37 ℃ for 24 h in the brain–heart infusion (BHI) broth (BD, Sparks, US). After disinfection, the discs

were transferred into a 48-well plate. Then, 990 μL of fresh BHI broth containing 1% sucrose (S8270; Solarbio, China) and 10 μL of *S. mutans* suspension (adjusted to 10^8 CFU/mL) were added to each well. The 48-well plates were then incubated at 37 ℃ micro-aerobically (5% CO_2, 1% O_2) for 24 h to form *S. mutans* biofilm on resin discs.

2.5.3. Colony-forming units (CFU) evaluation

After being gently rinsed with PBS, specimens were transferred into Eppendorf tubes with 1 mL sterile PBS respectively for CFU evaluation. The biofilm was dispersed by vortex-mixing for 3 mins, and the tenfold gradient dilution was performed. BHI agar medium (BHI broth with 15 g/L agar) was utilized for counting the number of *S. mutans* colonies from each culture dish (NEST Biotechnology, China). For each resin disc, three replicates were performed.

2.5.4. MTT assay

For the MTT assay, the discs covered with biofilms were gently rinsed with PBS three times to remove non-adherent *S. mutans*. Afterward, specimens were transferred into a new 48-well plate, and 1 mL solution of 3-(4,5-dimethyl-2-thiazolyl)-2,5-diphenyl-2-H-tetrazolium bromide (MTT, Sigma, US; 0.5mg/mL,) was dropped into each well. After incubating at 37 ℃ for 2 h micro-aerobically, the MTT solution was removed and replaced by 1 mL dimethyl sulfoxide (DMSO). The 48-well plate was then gently oscillated in the dark for 20 mins to dissolve formazan crystals. The OD_{540} value of the supernatant was measured using a spectrophotometer (Powerwave 340, Bio-Tek Instrument, US), and the relative biofilm vitality (RBV) was calculated as follows(Yan et al., 2017):

$$\mathrm{RBV} = \frac{\text{Absorbancy of experimental group}}{\text{Absorbancy of control group}} \times 100\%$$

2.5.5. Lactic acid measurement

For lactic acid measurement, the discs covered with biofilms were gently rinsed with cysteine peptone water (Sigma-Aldrich, US) to remove non-adherent *S. mutans* and then transferred into a new 48-well plate. 1.5 mL buffered peptone water (BPW) with 0.2% sucrose was added to each well, and the 48-well plate was then incubated at 37 ℃ for 3 h(Wang et al., 2019a). After incubation, the lactic acid concentrations in the BPW solutions were determined using a lactate dehydrogenase enzymatic method, and the OD_{340} value

was measured using the spectrophotometer(Wang et al., 2019a). Standard curves were prepared with the lactic acid standard (Supelco Analytical, US).

2.5.6. Scanning electron microscopy (SEM) observation

SEM observation was performed to detect the biofilm's morphology. After gently rinsed with PBS, the biofilms on each resin disc were fixed with 2.5% glutaraldehyde (0.1 mol/L cacodylate buffer, pH 7.2) in a new 24-ell plate. Afterward, the biofilms were dehydrated with gradient ethanol (30%, 50%, 70%, 80%, 90%, and 100%), desiccated for 48 h, sprayed with gold and observed under the SEM (VEGA 3 LMU, TESCAN, Czech).

2.5.7. Confocal laser scanning microscopy (CLSM) observation

For CLSM observation, resin discs were transferred into a new 24-well plate after gently rinsing with PBS. Specimens were then stained by the live/dead bacterial viability kit (Molecular Probes, Invitrogen, US) for 15 mins. After gently rinsed with PBS, *S. mutans* biofilm was observed under confocal laser scanning microscopy (CLSM, FV1000, Olympus, Japan) at 40 × magnification. Live bacteria stained by SYTO-9 emitted green fluorescence under the excitation of 488 nm wavelengths, and dead bacteria stained by propidium iodide (PI) emitted red fluorescence under the excitation of 523 nm wavelength. Images were obtained by continuous scanning from the bottom to the top of the biofilm in the vertical dimension with a 2 μm interval. The 3D overlay image of the biofilm (full thickness) was reconstructed and analyzed with Imaris (Imaris 7.2.3, Bitplane, Switzerland).

2.6. Color and stain resistance

2.6.1. Color change of the experimental resin

Colors of the resin disks (Ø 6.5 mm, H 1 mm) were measured via the Commission International de l'Echairage (CIE) L*a*b* color scale (n = 18 for each group) (Xu et al., 2014). In this color scale, L* reveals luminosity from darkness to lightness, a* represents green-red chromaticity, and b* represents blue-yellow chromaticity(Hollis et al., 2015). The color measurement was performed in a dark room via a spectrophotometer (PR-655 SpectraScan, Photo Research, US) outfitted with MS-75 and SL-0.5 × lens. Before each measurement, the spectrophotometer was calibrated with a white reflectance standard tile. For each specimen, L*a*b* values were continuously measured for three times, and the

mean value was calculated (L, a, b). The mean L*a*b* values of the control group were considered the baseline value (L_A, a_A, b_A). Color change (ΔE) after the incorporation of $aZnO_{QDs}$ and CHX@MSN of the four experimental groups was calculated as follows(Hollis et al., 2015):

$$\Delta E = [(L - L_A)^2 + (a - a_A)^2 + (b - b_A)^2]^{1/2}$$

2.6.2. Stain resistance measurement

Eighteen specimens of each group were randomly divided into three subgroups (n = 6). For each subgroup, specimens were stored in the staining solution composed of 40 mL of coffee (Costa Latte Caramel, Costa, UK), cola (Pepsi Cola, Pepsi, US), or tea (SUNTORY Oolong Tea, SUNTORY, Japan), respectively in a 37 ℃ incubator in darkness. The staining solution was replaced every day. A twelve-day laboratory staining was conducted to simulate a one-year clinical staining(Ardu et al., 2010). After the staining procedure, the specimens were cleaned in an ultrasonic cleaner for 5 mins and then dried with the paper towel. Similarly, L*a*b* values were measured three times for each specimen, and the stained mean value was collected ($L_{coffee/cola/tea}$, $a_{coffee/cola/tea}$, $b_{coffee/cola/tea}$). Color change ($\Delta E_{coffee/cola/tea}$) after staining was calculated as follows(Hollis et al., 2015):

$$\Delta E_{coffee/cola/tea} = \left[\left(L_{coffee/cola/tea} - L\right)^2 + \left(a_{coffee/cola/tea} - a\right)^2 + \left(b_{coffee/cola/tea} - b\right)^2\right]^{1/2}$$

2.7. Degree of conversion

The degree of conversion of the attachment resin was analyzed by FT-IR spectra (Nicolet 5700, ThermoFisher, US) equipped with a single reflection horizontal attenuated total reflectance (ATR) accessory. A very thin layer of uncured resin was placed on the ATR crystal, and the uncured samples' FT-IR spectra were collected (n = 6). Each specimen was then cured for 40 s, and the FT-IR spectra of the cured specimens were then collected again.

The degree of conversion was determined from the ratio of peak absorption of aliphatic C=C (peak at 1638 cm^{-1}) and aromatic C-C (peak at 1608 cm^{-1}) before and after curing as follows(Alshali et al., 2013):

$$\text{Degree of Conversion} = \left[1 - \frac{\left(\frac{1638\text{cm}^{-1}}{1608\text{cm}^{-1}}\right)\text{Peak height after curing}}{\left(\frac{1638\text{cm}^{-1}}{1608\text{cm}^{-1}}\right)\text{Peak height before curing}}\right] \times 100\%$$

2.8. Depth of cure

The curing depth of the resin was analyzed according to ISO 4049-2019 (ISO, 2019). The resin was evenly packed into a stainless-steel mold with a cylindrical cavity of 10 mm in height and 4 mm in diameter and then light cured (Bluephase Style, Ivoclar-Vivadent Amherst, US) from one side for 20 s. The samples were then taken out, and the uncured resin composite was immediately scraped off from the bottom with a plastic spatula. The depth of cure of each cylinder was measured by a digital micrometer from 5 different directions (n = 6, accurate to 0.01 mm).

2.9. Polymerization shrinkage

Eight small spheres with a diameter of approximately 3 mm were made for each group and then kept in the dark. Micro-CT scans were performed (Skyscan 1276, Bruker, Kontich, Belgium) before and after photo-polymerization (Sun and Lin-Gibson, 2008). Photo-polymerization was performed perpendicular to the specimens' surface with the LED light curing device for 40 s. The scanning operating conditions were 60 kV voltage, 200 μA current, 16 μm voxel dimensions, and the rotation step of 0.5°. All acquired raw images were reconstructed and analyzed with the software (NRecon v.1.6.10.2, Bruker, US; CTAn v. 1.15.4.0, Bruker, US). The polymerization shrinkage was determined as a percentage difference between the initial volume (before light curing) and the final volume (after light curing).

2.10. Water sorption and solubility

Eight resin disks (Ø 6.5 mm, H 1 mm) of each group were dried in a desiccator until a constant weight (m_0) had been achieved. The disks were stored in distilled water for seven days in an incubator at 37°C. After being blot dried, the disks were weighed again (m_1) within 30 s to eliminate the influence of desiccation. Then the specimen was oven-dried at

37 ℃till the equilibrium had been reached, after which a stable weight (m_2) was obtained.

Water absorption and solubility were calculated by(Yan et al., 2017):

$$\text{Water sorption rate} = \frac{m_1 - m_0}{m_0} \times 100\%$$

$$\text{Solubility rate} = \frac{m_0 - m_2}{m_0} \times 100\%$$

2.11. Softening in solvent

Ten resin discs (Ø 6.5 mm, H 1 mm) of each group were prepared for the test. Initial surface microhardness (SMH1) was measured via the micro-hardness tester (HX-1000TM, Taiming, China)(Yan et al., 2022a). Specimens were then immersed in a solution composed of ethanol (70%) and sterile deionized water (30%) for 2 h(Garcia et al., 2016). The softened surface microhardness (SMH2) was then tested. Softening rate was calculated as follows:

$$\text{Softening rate} = \frac{\text{SMH1} - \text{SMH2}}{\text{SMH1}} \times 100\%$$

2.12. Flexural strength (FS) and flexural modulus (FM)

FS and FM were determined via three-point bending test. According to ISO 4049-2019, six specimens of each group were prepared in a metal mold (25 mm × 2 mm × 2 mm) and light cured for 20 s in four separate overlapping portions (ISO, 2019). After being stored in distilled water at 37 ℃ for 24 h, the width and the height of the specimens were measured with the digital micrometer (accurate to 0.01 mm)and the specimens were loaded in a universal testing machine (E1000, Instron, England) at 1.0 mm/min crosshead speed.

Flexural strength (FS) was calculated by

$$FS = \frac{3F \times L}{2b \times h^2}$$

Flexural modulus (FM) was calculated by

$$FM = \frac{S \times L^3}{4b \times h^3}$$

Where F is the maximum load (N) exerted on the specimen, L is the length of the support span (20 mm), b is the width of the specimen (mm), h is the height of the specimen (mm), and S is the slope of the linear part of the stress-strain curve (N/mm).

2.13. Shear bond strength and SEM observation of the bonding interface

2.13.1 Sample preparation

Human maxillary premolars extracted for orthodontic reasons were collected after approval by the Ethics Committee for Human Studies of the School & Hospital of Stomatology, Wuhan University (No. 2019-A65). Premolars with caries, cracks, enamel anomalies or restorations were excluded. One hundred and seventy maxillary premolars were obtained and randomly divided into five groups (n = 34). After extraction, the teeth were cleaned to remove all gingiva, plaque, and odontolith, rinsed under running deionized water for 5 mins, and then kept in 0.1% thymol at 4 °C until the bonding procedure(Vianna et al., 2016).

Clear aligner attachment templates (Invisalign, US) from our finished Invisalign patients (Department of Orthodontics, Hospital of Stomatology, Wuhan University) were obtained after getting the patients' informed consent. Only the templates with rectangular attachments (height 2 mm, width 3 mm, depth 1 mm) designed on the maxillary premolars were selected. The corresponding parts were then cut off as our templates. The experimental resin was applied following the manufacturer's instructions (Filtek Z350XT, 3M ESPE, US). The crowns were cleaned with fluorine-free toothpaste for 10s. The buccal surface was then etched with 37% phosphoric acid for 30 s, thoroughly rinsed for 5 s, and dried with an air gun until the frosty white appearance was visualized. A thin coat of Single Bond Universal Adhesive (3M ESPE, US) was applied on the tooth surface and then light cured for 10 s. The template filled with the experimental resin was compressed onto the tooth surface and light cured for 30 s. Finally, the template was carefully removed, and the excessive resin surrounding the attachment was removed. The whole bonding process was conducted by the same researcher (LY Cao).

2.13.2 Shear bond strength (SBS) test

Thirty bonded teeth from each group were randomly picked for SBS test. The teeth were then randomly divided into two subgroups, immediate and long-term subgroup. Before the SBS test, roots were embedded in the epoxy resin base with buccal surfaces perpendicular to the base. For the immediate subgroup, bonded teeth were stored in

distilled water at 37 °C for 24 h. For the long-term subgroup, teeth were exposed to thermal cycling from 5 ℃ to 55 ℃ for 5000 cycles, with an immersion time of 30 s and a transit time of 15 s. SBS was measured via the universal testing machine (E1000, Instron, England) at a crosshead speed of 0.5 mm/min. A knife-edged blade was placed vertically to the occlusal surface of the attachment, in an occlusogingival direction parallel to the bonding interface. The maximum shear force (F_{max}) was recorded, and the SBS was calculated as follows:

$$\mathrm{SBS} = \frac{\mathrm{F}_{max}}{\mathrm{S}}$$

Where S is the area of the attachment base (6 mm^2).

2.13.3 SEM observation of the bonding interface

The remaining four bonded teeth from each group were used for SEM (MIRA, TESCAN, Czech) observation. Similarly, each group was further randomly divided into two subgroups. The aging method of the long-term subgroup was identical to the SBS test. All bonded teeth were sectioned vertically to the long axis of teeth and the center of attachments using a water-cooled diamond saw. Discs of 1 mm thickness were then rinsed in distilled water and vacuum dried at room temperature for three days. The discs were gold-sputtered, and the morphological evaluation of the resin-enamel bonding interface was conducted.

2.14. Cytotoxicity

2.14.1. Cell culture and resin extracts preparation

Human gingival fibroblasts (HGFs, ScienCell, US) were cultured with α-Modified Eagle's Medium (aMEM, Gibco, US) containing 10% fetal bovine serum (FBS; Gibco, US) and 1% penicillin-streptomycin (Invitrogen, US) at 37°C in a humidified atmosphere with 5% CO_2. Resin disks (Ø 8mm, H 1mm, n = 6) of each group were sterilized with 75% alcohol for 30 mins and rinsed with PBS three times. Extracts of the specimens were obtained using the ratio of 1.25 cm^2/mL according to ISO 10993-5 (ISO, 2009), which means that each specimen was immersed in 1 mL of aMEM containing 10% fetal bovine serum and 1% penicillin-streptomycin at 37°C for 24 h.

2.14.2. CCK-8 assay

HGFs were seeded in 96-well plates at a density of 8 ×10^3 cells/well and incubated at 37°C with 5% CO_2 for 48 h. After removing the culture medium, HGFs were incubated for another 24 h with 100 μL extracts per well at 37 ℃ with 5% CO_2. Five repetitions were set for each extract. The natural culture group (Group NC) was set by incubating the HGFs with 100 μL culture medium alone. After that, 10 μL CCK-8 solution (CCK-8 kit, Beyotime, China) was added to each well and incubated for 2 h at 37 ℃ with 5% CO_2. Absorbance was measured at 450 nm using the spectrophotometer. Relative cell vitality (RCV) was calculated as follows:

$$\mathrm{RCV} = \frac{\text{Absorbancy of exctract group}}{\text{Average absorbancy of Group NC}} \times 100\%$$

2.14.3. Live/dead cell staining

For live/dead cell staining, HGFs were seeded in 48-well plates at a density of 2.4 ×10^4 cells/well and incubated at 37°C with 5% CO_2 for 48 h. Then, 250 μL of the rest extracts was dropped into each well. Group NC was also set with only culture medium. After 24 h incubation at 37 ℃ with 5% CO_2, the 48-well plate was washed by PBS for three times and stained with Calcein AM/PI Cell Vitality/Cytotoxicity Assay (Beyotime, China) for 30 mins in the dark condition at 37 ℃ with 5% CO_2. Calcein-AM/PI staining images were photographed by an inverted fluorescence microscope (Eclipse Ti-E, Nikon, Japan) and then merged (Image J, National Institutes of Health, US). Live cells presented staining with green fluorescence under the excitation of 494 nm wavelength, and dead cells presented staining with red fluorescence under the excitation of 523 nm wavelength.

2.15. Fluorescence capability

Based on the results of the tests above, AFAR-2 group exhibited long-lasting antibacterial ability without comprising its mechanical properties. Therefore, only the control group, FAR, AFAR-2 group were tested. Resin discs (n = 2, Ø 10.5 mm, H 1 mm) of each group were polished with 800-, 1000-, and 2000-grit SiC sandpapers under running water and dried. Fluorescence intensity tests of the specimens were conducted with the

fluorescence spectroscopy (QuantaMaster 8000, HORIBA, Canada). Afterward, the resin discs were reclaimed and stored at 5 mL weekly replaced artificial saliva for six months at 37 ℃. Then, fluorescence intensity tests were conducted again for the resin discs. Moreover, photos of the resin discs under the mixing light (natural light + ultraviolet light) were taken. Photos of the bonded attachments (control group, FAR, AFAR-2) on the premolars were also obtained under the mixing light.

2.16. Statistical analysis

CFU evaluation, MTT assay, lactic acid measurement, color-related data, polymerization shrinkage, depth of cure, FS and FM, softening rate, water sorption and solubility, degree of conversion, SBS, and CCK-8 assay results were shown in mean ± SD and analyzed using one-way ANOVA and Tukey's multiple comparison tests. The significance level for all tests was set at $\alpha = 0.05$.

3. Results

3.1. Characterization of $aZnO_{QDs}$, pMSN, and CHX@pMSN

The characterization of $aZnO_{QDs}$ is displayed in **Fig. 1**. Spherical-shaped $aZnO_{QDs}$ were obtained (**Fig.1 A**). High-resolution TEM observation of $aZnO_{QDs}$ showed clear lattice fringes, and the size of $aZnO_{QDs}$ was around 6 nm (**Fig.1 B**). FT-IR spectra (**Fig.1 C**) indicated that both normal ZnO and $aZnO_{QDs}$ had an absorption peak around 450 cm^{-1} that belongs to the Zn-O functional group(Winiarski et al., 2018). The 3400 cm^{-1} absorption peak was from the O-H stretching vibration of bound water. Zn–O–Si and Si–O–Si symmetrical stretching vibration bands at 1100 cm^{-1} and 1010 cm^{-1} were observed in $aZnO_{QDs}$, indicating that the success amino-silane functionalization of ZnO_{QDs} via covalent chemical bonds(Lee et al., 2014). The XRD pattern (**Fig.1 D**) exhibited high intensity peaks of $aZnO_{QDs}$, corresponding well to the crystallographic planes of wurtzite zinc oxide (JCPDS 36–1451)(Talam et al., 2012). The fluorescence spectra (**Fig. 1 E**) presented a narrow peak of excitation spectrum around 360 nm, and a strong band of emission spectrum peaked around 550 nm. The $aZnO_{QDs}$ powder (**Fig. 1 F**) was white under natural

light and could emitt strong yellowish fluorescence under ultraviolet light and mixing light.

The characterization of pMSN and CHX@pMSN are displayed in **Fig. 2**. TEM showed that pMSN were typical spherical with a diameter of about 100 nm, and the regular hexagon micro-porosities were evenly distributed (**Fig.2 A**). After the loading of CHX, the structure of mesopores became obscured and less clear (**Fig.2 B**). Element mapping revealed the existence of silicon, oxygen, and chlorine in CHX@pMSN (**Fig.2 C**). The strong chlorine signal in and around the pMSN particle indicated the coverage and infiltration of CHX into the pMSN. FESEM images showed that the pMSN (**Fig.2 D**) and CHX@pMSN (**Fig.2 E**) were both in a spherical shape, and the CHX@pMSN exhibited smoother surfaces and generally larger size.

The FT-IR spectra of pure CHX, CHX@pMSN and pMSN were presented in **Fig.2 F**. The characteristic peak of the Si-O-Si group at 1082 cm^{-1} was presented in pMSN and CHX@pMSN(Akram et al., 2021; Wu et al., 2017). Both pure CHX and CHX@MSN exhibited characteristic peak at 725 cm^{-1}, 1533 cm^{-1} and 2947 cm^{-1}, which can be assigned to -CH_2, C-H and C=N bond of CHX(Akram et al., 2021; Wu et al., 2017). Small angle XRD (**Fig.2 G**) showed a strong diffraction peak of the crystal face (100) and the other two characteristic peaks of crystal faces (110 and 200) of pMSN. However, the characteristic peak of the CHX@pMSN was not obvious. The thermogravimetric analysis (TGA) and differential thermal analysis (DTA) are presented in **Fig.2 H**. The TGA reveals a significant weight loss of CHX@pMSN from 150 ℃ to 500 ℃, and the loading amount of CHX was calculated as 50.13 wt.% to the total weight of CHX@pMSN. As the DTA suggests, both pMSN and CHX@pMSN exhibited a small endothermic peak around 48 ℃, which might be attributed to the evacuation of physically adsorbed water. For CHX@pMSN, the endothermic peak at 192 ℃ might corresponds to the evaporation of physically attached CHX on pMSN, and the endothermic peak at 470 ℃ might refer to the decomposition of the intercalated CHX within the pMSN(He et al., 2006; Yan et al., 2017). The nitrogen adsorption-desorption ion analysis (**Fig.2 I**) indicated that the pMSN and the CHX@pMSN exhibited a type IV isotherm, suggesting the presence of mesopores. Both pMSN and

CHX@MSN showed the type H1 hysteresis loop, but the hysteresis loop of pMSN was much more obvious. The specific surface area, pore volume, and pore diameter decreased after incorporating CHX (**Table 1**).

3.2. CHX release

The cumulative release profiles of CHX from the modified attachment resin discs of AFAR-1, AFAR-2, and AFAR-3 from 1 day to 30 days are presented in **Fig. 3**. A sudden release at day 1 was observed, then the release speed gradually slowed down and was kept at a stable level to day 30. With the increase of the content of CHX@pMSN of the resin discs, the cumulative CHX release was elevated correspondingly at each time point.

3.3. Antibacterial activities

3.3.1. CFU counting, MTT assay, and lactic acid production inhibition

The inhibitory effects of the attachment resins on *S. mutans* biofilm colony reproduction and the metabolic activities from the CFU and the MTT assays are presented in **Fig. 4** and **Fig. 5 A**. For the immediate subgroup, all the four experimental groups exhibited significantly decreased biofilm metabolic activities as the MTT assay suggested ($P < 0.05$), while only AFAR-1, AFAR-2, and AFAR-3 groups showed significant decreases of *S. mutans* colony reproduction as the CFU suggested ($P < 0.05$). For the 1-week subgroup, there was no statistical difference between the control group and the FAR group ($P > 0.05$), irrespective of the CFU or the MTT assay. But the AFAR-1, AFAR-2, and AFAR-3 still presented significant decreases in colony reproduction and the metabolic activities of the *S. mutans* biofilms ($P < 0.05$). For the 1-month subgroup, the inhibitory effect of AFAR-1 group was partially depleted but still significant ($P < 0.05$), and the antibacterial ability remained strong for AFAR-2 and AFAR-3 groups ($P < 0.05$).

Biofilm lactic acid production of each group is plotted in **Fig. 5 B**. Lactic acid production was significantly suppressed in all the experimental groups immediately ($P < 0.05$), while the AFAR-1, AFAR-2, and AFAR-3 exhibited the strongest inhibitory effects. After 1-week aging, no significant difference was observed between the control group and FAR group ($P > 0.05$), but the lactic acid production of AFAR-1, AFAR-2, and AFAR-3 groups remained

significantly lower than the control group ($P < 0.05$). After 1-month aging, similar to the MTT result, the inhibitory effect of AFAR-1 group on lactic acid production was partially consumed ($P < 0.05$), but the AFAR-2, and AFAR-3 groups remained strong.

3.3.2. SEM and CLSM observation of biofilm inhibition

The *S. mutans* biofilm growth on resin discs from representative SEM images is presented in **Fig. 6**. The control group and the FAR group both showed thick and extensive biofilms, covering the entire surface of the resin discs. For the immediate subgroup and 1-week subgroup, the surfaces of AFAR-1, AFAR-2, and AFAR-3 were only attached with scattered and deformed bacteria, with no biofilm formed. After 1-month of aging, a thin layer of *S. mutans* biofilm was formed on the surface of AFAR-1, while AFAR-2 and AFAR-3 remained low levels of bacteria adhesion.

The *S. mutans* biofilm growth on resin discs from 3D overlay CLSM images and the corresponding biomass distribution of live/dead bacteria in each layer are exhibited in **Fig. 7**. The control group and the FAR group both showed thick *S. mutans* biofilms on their surfaces with large quantities of the live and total bacteria. For AFAR groups, not only the thickness of the biofilms was greatly decreased but also the total volume of germs was largely reduced. With the increase of the addition of the CHX@pMSN, there was a decreasing tendency of the volume and the thickness of the biomass. And with the elongation of the storage time, the volume and the thickness of the biomass slightly increased for the AFAR-2 and AFAR-3 groups, but remained at a fairly low stage compared with the control group. However, the AFAR-1 group displayed an apparent upward trend in *S. mutans* biomass, similar to the results in SEM observation.

3.4. Color change and stain resistance

The effect of the incorporation of $aZnO_{QDs}$ and CHX@pMSN on the color of attachment resin is listed in **Table 2**. Color change at $\Delta E > 3.3$ is considered clinically perceptible(Mundim et al., 2010). The incorporation of 3 wt.% $aZnO_{QDs}$ alone did not cause significant or perceptible color change ($\Delta E = 1.99$, $P > 0.05$). But the a* value exhibited a significant tendency of increasing, indicating a shifting trend toward the red color direction ($P < 0.05$). For AFAR-1 group, the further incorporation of 1 wt.% CHX@pMSN only leads

to a significant increase in the a* value. For AFAR-2 group, the incorporation of 3 wt.% CHX@pMSN caused a significant color change, but was still under the 3.3 clinically perceptible threshold (ΔE = 2.90, $P < 0.05$). And the further incorporation of 3 wt.% CHX@pMSN also lead to a significant increase of the b* value, suggesting a shifting trend towards the yellow color direction ($P < 0.05$). For AFAR-3 group, with further addition of 5 wt.% CHX@pMSN, the color change became significant and clinically perceptible (ΔE = 5.26, $P < 0.05$), and the L* value decreased significantly, indicating a lower luminosity of the resin ($P < 0.05$).

The mean ΔE values and standard deviations of all groups in different staining solutions are listed in **Table 3**. In tea and coffee, all the five groups exhibited clinically perceptible color change after twelve days of staining (ΔE > 3.3), but there was no statistical difference between the groups ($P > 0.05$). For the staining solution of cola, with the increasing incorporation of CHX@pMSN, AFAR groups showed a decreasing tendency of the ΔE values, which were all below the 3.3 clinically perceptible threshold. Compared with the control group, AFAR-3 had the strongest anti-cola-staining capability (ΔE = 2.32, $P < 0.05$).

3.5. Degree of conversion and depth of cure

The result of degree of conversion is presented in **Fig. 8 A**. No statistical difference was found between the groups ($P > 0.05$). The depth of cure is plotted in **Fig. 8 B**. It could be seen that as the incorporated content increased, the depth of cure notably decreased, and all the four experimental groups exhibited significant difference with the control group ($P < 0.0001$).

3.6. Polymerization shrinkage

The volume shrinkage percentages of the attachment resins are plotted in **Fig. 8 C**. It could be found that as the incorporation of the CHX@pMSN increased, the polymerization shrinkage rate decreased, while only AFAR-3 exhibited statistical difference with the control group ($P <0.05$).

3.7. Water sorption and solubility

Water sorption and solubility of the five groups are presented in **Fig. 8 D** and **E**. With increasing incorporation amount of CHX@pMSN, the water sorption rate tended to increase, but only AFAR-3 group exhibited statistical difference with the control group and the FAR group ($P < 0.05$). Besides, no significant difference in solubility rate was found among all groups ($P > 0.05$).

3.8. Softening in solvent

Softening in solvent rates are presented in **Fig. 8 F**. All groups showed decreased values of surface micro-hardness after immersing in the ethanol-water solution. AFAR-1 group showed the lowest softening rate. With the further incorporation of CHX@pMSN, the softening rate significantly increased in AFAR-3 compared to AFAR-1 ($P < 0.05$). However, compared to the control group, none of the four experimental groups exhibited statistical difference ($P > 0.05$).

3.9. Flexural strength (FS) and flexural modulus (FM)

FS and FM of the five groups are displayed in **Fig. 9**. Compared to the control group, only AFAR-3 group exhibited significantly decreased the values of FS and FM in the three-point flexural test ($P < 0.05$).

3.10. Shear bond strength (SBS) and SEM observation of the boding interface

The assessment of the SBS of clear aligner attachment and immediate/long-term SBS values are shown in **Fig. 10 A**, **B**, and **C**. For the immediate subgroup, only AFAR-3 showed statistically significant decrease in SBS value with the control group ($P < 0.05$). After 5000-cycles of thermal cycling, the long-term SBS values of the FAR, AFAR-1, and AFAR-2 groups were still comparable to that of the control group ($P > 0.05$), whereas AFAR-3 group showed significantly lower SBS ($P < 0.05$).

The morphology of the resin-enamel bonding interfaces is presented in **Fig. 10 D**. The SEM images of the control group, FAR, AFAR-1 and AFAR-2 showed compact bonding

interfaces with no evident gap before and after the aging process. For AFAR-3, before the aging process, the contact between the enamel and the resin was also compact. However, after the thermal cycling process, some small gaps (as the red arrows point) were presented at the resin-enamel bonding interface.

3.11. Cytotoxicity

CCK-8 assay (**Fig. 11 A**) indicated that no significant difference in the relative cell viability of HGFs among the five groups ($P > 0.05$). Live/dead cell staining results (**Fig. 11 B**) also showed no significant difference among the four experimental groups and the control group in the number and morphology of the green fluorescent HGFs.

3.12. Fluorescence intensity

The fluorescence spectrophotometer (**Fig. 12 A** and **B**) showed that the resin discs of FAR and AFAR-2 groups emitted a strong band of fluorescence peaked around 550 nm. Adding 3 wt.% of CHX@pMSN did not remarkably weaken the resin's fluorescence intensity, and the fluorescence intensity did not dramatically decrease within six months. Besides, the fluorescence of Filtek Z350 (control group) was also detected, which emitted relatively weak blue light peaked around 495 nm. The photos of the FAR and AFAR-2 resin discs (**Fig. 12 C**) presented strong yellowish fluorescence without apparent attenuation over six months under the mixing light (natural light + ultraviolet light). When bonded on the tooth surfaces (**Fig. 12 C**), under the mixing light, the attachment of the control group did not exhibit apparent differentiation with enamel, while FAR and AFAR-2 exhibited strong yellowish fluorescence.

4. Discussion

WSLs is one of the most common side effects of orthodontic treatment(Huang et al., 2022; Yan et al., 2022b). Recent study revealed that the incidence of WSLs reached 41.18% among the patients undergoing clear aligner treatment(Alshatti, 2017). Long-time wearing of clear aligners would limit the flow of saliva, thus impairing the cleansing, buffering, and remineralization effects of the saliva(Albhaisi et al., 2020; Moshiri et al., 2013). Cleansing

activities of lips, cheeks, and tongue are also constrained, leading to the further entrapment and development of the biofilms underneath the aligners(Moshiri et al., 2013). Enamel WSLs are more likely to appear around the bonded attachments, as the food and bacteria could get easily accumulated around these retention sites created by protruded attachments, where are not normally considered prone to caries(Albhaisi et al., 2020; Low et al., 2011; Moshiri et al., 2013). Currently, studies focusing on clear aligner technology are constantly getting enriched, whereas researches regarding the clear aligner attachment remain sparse(Chen et al., 2021). The present research aimed to explore the feasibility of incorporating $aZnO_{QDs}$ and CHX@pMSN to modify a routinely-used clear aligner attachment resin with fluorescence capability and long-term antibacterial activities. Thus, the clear-aligner-related WSLs could be prevented and it would be easier for orthodontists to distinguish between the resin and the enamel when removing the attachments at the end of the treatment. According to the results above, the immediate and long-term antibacterial activities and fluorescence capability of AFAR-2 were proved. Moreover, the incorporation of 3 wt.% $aZnO_{QDs}$ and 3 wt.% CHX@pMSN (AFAR-2 group) did not compromise the esthetic property, biocompatibility and mechanical performance of the attachment resin. Therefore, all the five null hypotheses were rejected.

In this research, $aZnO_{QDs}$ were synthesized using the sol-gel method according to our previous study and got further amino-silane functionalized to promote bonding with the resin and enhance the biocompatibility(Yan et al., 2022a; Zhao et al., 2013). TEM (**Fig.1 A** and **B**) showed spherical-shaped 6-nm-sized $aZnO_{QDs}$ were synthesized. Unique sharp peak in the fingerprint area of FT-IR spectra (**Fig.1 C**) around 450 cm^{-1} proved the existence of the Zn-O bond and the Si–O–Si stretching vibration band around 1010 cm^{-1} proved successful amino-silane functionalization(Lee et al., 2014; Winiarski et al., 2018). Characteristic peaks of $aZnO_{QDs}$ in the XRD pattern (**Fig.1 D**) corresponded well to the Joint Committee on Powder Diffraction Studies Standards (JCPDS, No. 36–1451) card, showing that our synthesized $aZnO_{QDs}$ had a wurtzite crystalline structure(Talam et al., 2012). Fluorescence spectrometer tests (**Fig.1 E**) and direct visual observation (**Fig.1 F**) certified the fluorescence ability of $aZnO_{QDs}$ and the fluorescence intensity was strong enough to be observed in the mixing light with the assistance of an ultraviolet radiator.

It has been reported that the current enamel remineralization therapies have limited effects on post-orthodontic WSLs, and also heavily rely on the patients' compliance (Hu et al., 2020; Hua et al., 2020; Hua et al., 2018). Bacterial control modification of the dental appliances, on the contrary, doesn't require patient compliance and is gradually becoming an exciting notion for the prevention of the WSLs (Wang et al., 2023). To prevent the formation of enamel WSLs from an antimicrobial perspective, the novel attachment resin was formulated to contain antibacterial agents in this study. Although ZnO nanoparticles indeed possess antibacterial ability, studies have reported that the effect is weak, short-lasted, and lacks peripheral impact, which can be attributed to their low solubility (Aydin Sevinc and Hanley, 2010; Tavassoli Hojati et al., 2013). Our previous studies have shown that adding up to 20 wt.% ZnO_{QDs} to orthodontic adhesive resin was necessary to achieve acceptable antibacterial properties (Yan et al., 2022a). While our preliminary experiments indicated that incorporation of 20 wt.% $aZnO_{QDs}$ into the attachment resin, which is much thicker than the adhesive resin, could negatively impact on its mechanical properties and did not possess long-term antibacterial effect. Therefore, the more widely applied antibacterial agent, CHX, was utilized in this study. In the field of dentistry, CHX was utilized in this study. Widely applied in the dental field, CHX has clear advantages against both $Gram^+$ and $Gram^-$ bacteria, and is less likely to develop antimicrobial resistance compared to antibiotics(Seneviratne et al., 2014; Yan et al., 2018; Yan et al., 2017). To achieve long-term antibacterial activity, CHX was further loaded in the nanocarrier—MSN, and then CHX@pMSN was incorporated into the attachment resin.

In this study, pMSN was synthesized by applying the swelling agents—TMB to the CTAB-templated sol–gel reaction(Yan et al., 2018). TEM (**Fig.2 A**) showed the 100-nm-sized spherical pMSN with highly regular mesopores, comprising a hexagonal array typical of MCM-41 type MSN(Yang et al., 2017). The structure of mesopores of CHX@pMSN became obscured and less clear, and the element mapping revealed strong chlorine signal in CHX@pMSN, suggesting successful loading of CHX (**Fig.2 B** and **C**). FESEM (**Fig.2 D** and **E**) showed the spherical-shaped pMSN and CHX@pMSN, and the CHX@pMSN exhibited a smoother surface and relatively larger size. FT-IR spectra (**Fig.2 F**) and small angle XRD (**Fig.2 G**) also showed successful synthesis of pMSN and loading of CHX. By

elongating the loading time and increasing the concentration of the CHX diacetate salt hydrate in the ethanol solution, the loading amount of CHX reached 50.13 wt.% as the TGA revealed (**Fig.2 H**). The nitrogen adsorption–desorption analysis (**Fig.2 I** and **Table 1**) revealed decreased specific surface area, pore volume, and pore diameter after the loading of CHX, but the CHX@pMSN still showed a type IV isotherm. The perfect channel architecture, high surface area, high pore volume, and high loading amount made the pMSN an advantageous nanocarrier for CHX.

The application of CHX@MSN has aroused great interest in the field of dentistry in recent years. Seneviratne et al. revealed the potent antibacterial ability of the CHX@MSN on both planktonic bacteria and biofilms of various oral pathogenic bacteria(Seneviratne et al., 2014). Another study incorporated CHX@MSN into the dental composites and demonstrated the 24-hour antibacterial activity of the modified resin(Zhang et al., 2014). Yan et al. also incorporated CHX@MSN into the dentin adhesive and glass ionomer cement and achieved 30-day sustained antibacterial activity(Yan et al., 2018; Yan et al., 2017). The living bacteria present in mature biofilms always possess high resistance to antimicrobial agents compared to the planktonic bacteria (Seneviratne et al., 2014). Therefore, in this study, *S. mutans* biofilms, the major causative factor of the WSLs, were cultivated on the experimental resin discs to explore the antibacterial activity of the novel attachment resin.

As the results suggest, the antibacterial activity of the attachment resin modified by 3 wt.% aZnO_{QDs} alone (FAR group) was relatively weak and short, only exhibited a significant decrease of RBV and lactic acid production (**Fig.5**) in the immediate subgroup. The CHX@pMSN incorporated attachment resin (AFAR groups) exhibited obvious immediate and long-term antibacterial activity as the results suggested. The expected long-term antibacterial capability largely depends on the sustained release of CHX from pMSN. In this study, the CHX release (**Fig.3**) was directly detected from resin discs of AFAR groups instead of the CHX@pMSN powders, thus the actual release pattern of the attachment resin could be assessed. The time points of the aging process were all included in the CHX release test. The relative stability of both the CHX concentration and the solution volume was maintained throughout the test, which was designed to simulate the oral cavity

environment as closely as possible. Release pattern showed that CHX@pMSN modified attachment resins possessed up to one month of sustained release of CHX, and the attachment resin with a higher content of CHX@pMSN exhibited a stronger release ability. These results were highly consistent with the results obtained from the antibacterial tests. Moreover, a sudden release at day 1 was observed, then the release speed gradually slowed down over time, consistent with the decrease in antibacterial properties after aging. The inhibition effect of AFAR groups on *S. mutans* biofilm was strong immediately and after the 1-week aging process. CFU (**Fig.4**) counting presented a significant decrease in colony reproduction by orders of magnitude, from 10^7 to 10^3, and the MTT assay (**Fig.5 A**) also showed that RBV was suppressed under 10%. For the formation of lactic acid (**Fig.5 B**) from the biofilms, the concentration was lowered to less than 0.3 mmol/L, revealing the suppressed acidogenicity of the bioflims. SEM images (**Fig.6**) showed only few scattered and deformed bacteria attached to the resin discs and no mature biofilm was formed. Full thickness of the biofilms of the Z-stack were recorded via CLSM. Thus, not only the distribution of the biomass from each layer could be recorded, but also the thickness of the biofilm could be estimated. CLSM (**Fig.7**) indicated that the thickness of biofilms was reduced from more than 30 μm to less than 12 μm, and the volume of live biomass and total biomass also greatly decreased. It could be inferred that most germs could have been killed by the released CHX before attaching to the resin discs. After 30 days of aging, the antibacterial effect of AFAR-1 got partially depleted, but AFAR-2 and AFAR-3 remained strong. The metabolic activity, acidogenicity, bacteria counting, biomass volume, and biofilm thickness all showed a significant decrease. From these results, it could be concluded that AFAR-2 and AFAR-3 possess strong and long-lasting antibacterial effects against *S. mutans* biofilms.

The esthetic property of the attachment resin is also of vital importance. Patients undergoing clear aligner treatment need to bond multiple attachments on teeth surfaces, including the esthetic zone of the front teeth(Feinberg et al., 2016). The color of the attachments should match the natural tooth as closely as possible. The CIE L*a*b* color scale system has been widely applied as an objective modality to judge the colorimetric properties of dental resins, which eliminates the subjective variability in color perception

and provides a standardized method to calculate color changes quantitatively(Xu et al., 2014). Color change at ΔE > 3.3 is considered clinically perceptible(Mundim et al., 2010). The result (**Table 2**) indicated that there was no statistical difference between the control group, FAR and AFAR-1 group. The AFAR-2 and AFAR-3 groups showed a significant increase of ΔE, but only the ΔE of AFAR-3 was considered clinically perceptible. This could be contributed to the opaque nature of the $aZnO_{QDs}$ and CHX@pMSN. Over-incorporation of these nanoparticles could lead to a lower luminosity of the resin as the results suggested.

Another important consideration of the clear aligner attachment is the resistance to staining. Unlike the plastic aligners, which could be removed before drinking or eating, the bonded attachments are directly exposed to dark-stain liquids and foods, causing staining of the aligner attachments. Discolored attachments in the esthetic zone could cause patients' dissatisfaction. The experimental attachment resins should not be more susceptible to staining than the commercial resin. In this study, the twelve-day continuous staining was designed to simulate one-year clinical staining(Ardu et al., 2010). And three worldwide heavily consumed beverages: coffee, tea, and carbonated drink (cola) were selected as the staining liquids. In this study, coffee and tea showed clinically perceptible staining of the attachment resin. The color change (**Table 3**) has a tendency of increasing with the further addition of CHX@pMSN but with no statistical difference for the samples immersed in tea and coffee. It might be contributed to the mesoporous nature of pMSN, which could cause higher absorption of pigmented beverages such as tea and coffee. Cola did not cause severe discoloration as tea and coffee. And the color change decreased with the further addition of CHX@pMSN for the samples immersed in cola. The discoloration of AFAR-3 was even below the clinically perceptible threshold and showed a significant difference with the control group. It has been demonstrated that, compared to tea and coffee, the carbonated drink—cola had the lowest pH which could damage the surface integrity of the resin, and why cola did not produce as much discoloration as coffee or tea could be contributed to its lack of yellow colorant(Malekipour et al., 2012). The incorporated CHX@pMSN nanoparticles increased the mass fraction of filler, which might enhance the surface integrity of the resin against the carbonated drink.

Moreover, the addition of CHX@pMSN and $aZnO_{QDs}$ in the attachment resin should

not interfere its polymerization process. After being light cured, the C=C in the uncured resin monomer gets opened and connected, referred to as the polymerization process, and the degree of conversion is the indicator of resin polymerization (Yan et al., 2022a). In this study, no significant difference in the degree of conversion (**Fig. 8 A**) was found between each group. The result suggested that the incorporation of 3 wt.% $aZnO_{QDs}$ and up to 5 wt.% of CHX@pMSN would not affect the degree of conversion of the attachment resin in the specimens with low thicknesses tested via FT-IR spectra. The depth of cure of the resins was tested according to ISO 4049-2019 (ISO, 2019). The results show a significant decrease in the depth of cure (**Fig. 8 B**) across all four experimental groups, compared to the control group. As the volume of incorporated nanoparticles increased, the curing depth decreased. However, this appears to be contradictory when compared to the degree of conversion. This distinction can be explained by the different measuring methods used. While the conversion degree was measured in a very thin layer of resin, the depth of cure required curing a 10-mm height resin. The $aZnO_{QDs}$ and the CHX@pMSN are opaque against visible light and when incorporated into the attachment resin, it would adversely affect the penetration of the curing light beam, especially for the thick specimens(Yan et al., 2018; Yan et al., 2022a). Despite this, all experimental groups exhibited a cured depth of more than 4 mm, which far exceeds the ISO standard of 1.5 mm (ISO, 2019). Furthermore, in clinical settings, the thickness of attachment resin for clinical usage does not exceed 2 mm, which is within the curing capability of all four experimental attachment resins.

In clear aligner treatment, tooth movement is realized by the mechanical perturbation induced by the aligner material, the programmed mismatch between the aligner, teeth and attachments in each step(Mantovani et al., 2019). To achieve efficient tooth movement, the clear aligner and the attachments should be tightly fit to transmit the orthodontic force to the teeth. The resin used for attachments should have relatively lower polymerization shrinkage to accurately restore the designated shape of the attachment. In the recent decades, micro-CT has been applied to effectively characterize the volume of polymeric dental composites before and after polymerization, thus allowing the determination of polymerization shrinkage (Sun and Lin-Gibson, 2008). Micro-CT provides fast acquisition

of high-resolution 3D images with the small objects. The utility and the accuracy of this method has been proved on multiple experimental and commercial materials (Ersen et al., 2020; Sun and Lin-Gibson, 2008). It is a non-destructive method that can provide accurate images regardless of the shape, physical states, and the position of the object, and can tolerate the artefacts caused by air bubbles within the resin and now has been widely accepted (Ersen et al., 2020; Rizk, 2022). With the increased mass fraction of filler, the polymerization shrinkage of the composite resin would be lower (Yang et al., 2022). The result of micro-CT (**Fig. 8 C**) indicated decreased polymerization shrinkage rate with the increased volume of the incorporated CHX@pMSN, which is beneficial for the accurate replication of the attachments on the enamel surface.

Considering that the oral cavity is a moisture condition, the clear aligner attachment resin polymer networks might absorb water and chemicals from their surroundings and also release components in turn (Ferracane, 2006). The dental material's high water sorption and solubility rate may lead to hydrolytic degradation, reducing its mechanical performance and shortening its service life (Toledano et al., 2003). The results showed a decreasing tendency of solubility and an increasing tendency of water sorption, but only AFAR-3 exhibited a significant difference in solubility compared to the control group and FAR group (**Fig. 8 D** and **E**). The decreased solubility could be contributed to the increased mass fraction of filler—CHX@pMSN, while the increased water sorption rate might result from the mesoporous structures of pMSN, which provided pathways for water to infiltrate into the attachment resin. For softening in the solvent test (**Fig. 8 F**), all the attachment resins showed degradations after immersing in the water-ethanol solution. The ethanol was absorbed in the resin, causing the structural expansion and leakage of uncured resin monomers, thus resulting in resin softening(Yan et al., 2022a). AFAR-1 and AFAR-2 showed decreased softening rates, suggesting CHX@pMSN might strengthen the resistance of the resin to degradation at an appropriate mixing ratio. This could be attributed to the inorganic nature of pMSN, which is less susceptible to solvents than the resin matrix. However, further incorporation of 5 wt.% CHX@pMSN (AFAR-3) showed an increase in softening rate but with no statistical difference compared with the control group. Over-incorporation of the CHX@pMSN might reduce the transmittance of resin during the

curing process, leading to an increased proportion of monomers and thus weakening the resistance to degradation.

Furthermore, the durability of clear aligner attachments is crucial, and it heavily relies on both mechanical strength and bonding strength. Clear aligner attachments must possess adequate mechanical and bonding strength to withstand masticatory loads and orthodontic forces lasting for more than a year (Barbin et al., 2020; Feinberg et al., 2016). Poor bonding between teeth and attachments, as well as weak mechanical strength, may result in frequent falling off or cracking of the attachments, leading to unplanned hospital visits, compromised treatment outcomes, and patient dissatisfaction. To determine the mechanical strength, the FS and FM were measured via the three-point bending test in this study. It was previously reported that incorporation of 4.5 wt.% of CHX@MSN slightly decreased the FS and FM of the resin (Zhang et al., 2014). In our study, the incorporation of $aZnO_{QDs}$ exhibited a positive effect on FS and FM while CHX@pMSN slightly decreased the values, but only AFAR-3 presented statistical significance (**Fig. 9**). The SBS test is believed to be a reliable method for analyzing the bonding strength of the composite resin on enamel (Chen et al., 2021). In this study, the thermal cycling aging protocol was referred to ISO/TS 11405:2015 standard but the cycle-index was increased from 500 to 5000 times, extrapolating for approximately 4.16 years of clinical service (ISO, 2015; Jurubeba et al., 2017). The immediate and long-term SBS (**Fig. 10 B** and **C**) showed no significant difference except for AFAR-3 group. SEM observations (**Fig. 10 D**) of the resin-enamel interfaces also indicated that only AFAR-3 presented some small cracks of the enamel-resin interfaces after 5000 thermal cycles, consistent with the results of the SBS test. We speculate that the decreased FS, FM, and SBS values of the AFAR-3 in this study might be attributed to the over-incorporation of CHX@pMSN. Previous studies have extensively explored the potential of silica-based nanoparticles as fillers for dental resins (Aati et al., 2022). It was demonstrated that MSN, with its large specific surface area, can significantly increase the viscosity of the resin matrix which limit equivalent presence of the content, thus adversely affecting the material's physical properties (Liu et al., 2021). Moreover, due to their high surface energy, over-incorporated MSNs have a tendency to aggregate in the resin matrix, creating stress concentrations in resin structure, therefore affecting its

consistency and further impairing the physical properties (Aati et al., 2022; Bai et al., 2020).

A biomedical material should have its biocompatibility assessed before the clinical transformation. The empty pMSN (MCM-41) employed in this research has long been proved to be a promising drug carrier with low cytotoxic potential(Tzankova et al., 2021; Yang et al., 2017). And CHX is also non-toxicity towards mammalian cells(Seneviratne et al., 2014). Our previous study also showed excellent histocompatibility and cytocompatibility of ZnO_{QDs}, while amino-silane functionalization of ZnO_{QDs} could further enhance its biocompatibility(Yan et al., 2022a; Zhao et al., 2013). Therefore, we speculated that the incorporation of $aZnO_{QDs}$ and CHX@pMSN in the attachment resin would not impair its biocompatibility. We obtained resin extracts as the culture medium and the HGFs were used as the target cells, which are the primary cells to contact the clear aligner attachments clinically. ISO 10993-5:2009, the biological evaluation of medical devices, was also strictly followed, which has been widely accepted for determining cytotoxicity of mammalian cells in vitro (ISO, 2009). Results of CCK-8 and live/dead cell staining (**Fig. 11**) proved our assumption. The modified resin did not show a significant decrease of RCV or an obvious change in HGFs cell number and morphology compared to Filtek Z350 XT.

Moreover, our study revealed that 3 wt.% $aZnO_{QDs}$ could endow the resin with strong yellowish fluorescence and the fluorescence of the resin remained strong and obvious even after six-month aging (**Fig.12**). Besides, the further incorporation of 3 wt.% CHX@pMSN did not weaken the fluorescence intensity of the experimental resin, whether immediately or after six-month aging. A recent research reported that the attachments could be identified via the fluorescence emitted from the commercial resin(Albertini et al., 2022). It was found in our study that Filtek Z350 XT indeed emitted blue fluorescence under the excitation of ultraviolet, but the fluorescence intensity was very faint compared with FAR and AFAR-2. In addition, visual observation (**Fig.12 C**) showed both the enamel and Filtek Z350 XT could emit similar blue fluorescence, making it hard to distinguish from each other. Studies have revealed that most of the restorative composite resins and the natural tooth enamel exhibited the similar color of the fluorescence (Kim et al., 2016; Lopes et al., 2021). A recent study reported that the fluorescence intensity of Filtek Z350 XT under ultraviolet was even weaker than natural tooth enamel (Lopes et al., 2021). The strong

yellowish fluorescence of FAR and AFAR-2 could help the professional to identify the resin and the enamel with the assistance of an ultraviolet radiator. Incomplete removal of the resin or the damages to the tooth enamel could thus be avoided.

According to the results, AFAR-2 exhibited long-term antibacterial activity and strong fluorescence capability, without compromising its esthetic properties, biocompatibility, and mechanical performances. The antibacterial activity of AFAR-2 could inhibit the biofilm formation around the attachments during clear aligner treatment, and its fluorescence capability could facilitate professionals to better discriminate the resin and the enamel when the attachments need to be removed. Therefore, the WSLs caused by biofilm accumulation around the attachments or unremoved resin remnants could be prevented, and the enamel damage resulting from the over-removal of the attachment resin could also be avoided. We presented a promising strategy to prevent the clear-aligner-associated WSLs without patients' compliance, and make attachment removal a much clearer process for the professionals. However, some limitations still exist in this study. As the clear treatment often takes more than a year, the antibacterial activity and fluorescence capability over a longer period of time still need to be tested under more realistic environments. Further research is also required to access the mechanical behaviors in more complex scenarios such as long-time storage and pH cycling. Long-term biocompatibility in the animal models will also be needed prior to its clinical and commercial translations.

5. Conclusion

In the present study, aZnO_{QDs} and pMSN were synthesized, and CHX was loaded into pMSN. We further incorporated aZnO_{QDs} and CHX@pMSN into the attachment resin to endow it with antibacterial activity and fluorescence capability. Test results suggested that the attachment resin incorporated with 3 wt.% aZnO_{QDs} and 3 wt.% CHX@pMSN showed long-term antibacterial ability, strong fluorescence capability, acceptable esthetic properties, good mechanical performances and satisfying biocompatibility. Based on these, the antibacterial and fluorescent attachment resin developed in this research is potentially applicable in the field of clear aligner treatment to prevent WSLs and facilitate professionals

to remove the attachment thoroughly and precisely.

Declaration of competing interest

The authors declare that they have no conflict of interest.

Acknowledgments

This work was supported by National Natural Science Foundation of China (No. 81901044), and the Chinese Stomatological Association COS Basic Research Fund (No. COS-B2021-08).

References

Aati, S., Aneja, S., Kassar, M., Leung, R., Nguyen, A., Tran, S., Shrestha, B., Fawzy, A., 2022. Silver-loaded mesoporous silica nanoparticles enhanced the mechanical and antimicrobial properties of 3D printed denture base resin. Journal of the mechanical behavior of biomedical materials 134, 105421.

Akram, Z., Aati, S., Ngo, H., Fawzy, A., 2021. pH-dependent delivery of chlorhexidine from PGA grafted mesoporous silica nanoparticles at resin-dentin interface. Journal of nanobiotechnology 19, 43.

Albertini, P., Tauro, R., Barbara, L., Albertini, E., Lombardo, L., 2022. Fluorescence-aided removal of orthodontic composites: an in vivo comparative study. Progress in orthodontics 23, 16.

Albhaisi, Z., Al-Khateeb, S.N., Abu Alhaija, E.S., 2020. Enamel demineralization during clear aligner orthodontic treatment compared with fixed appliance therapy, evaluated with quantitative light-induced fluorescence: A randomized clinical trial. American journal of orthodontics and dentofacial orthopedics : official publication of the American Association of Orthodontists, its constituent societies, and the American Board of Orthodontics 157, 594-601.

Alshali, R.Z., Silikas, N., Satterthwaite, J.D., 2013. Degree of conversion of bulk-fill compared to conventional resin-composites at two time intervals. Dental materials : official publication of the Academy of Dental Materials 29, e213-217.

Alshatti, H., 2017. Comparison of White Spot Lesions among Clear Aligners, Self-Ligating Brackets and Conventional Brackets-A Randomized Controlled Clinical Trial. University of Connecticut.

Anusavice, K.J., Zhang, N.Z., Shen, C., 2006. Controlled release of chlorhexidine from UDMA-TEGDMA resin. Journal of dental research 85, 950-954.

Ardu, S., Braut, V., Gutemberg, D., Krejci, I., Dietschi, D., Feilzer, A.J., 2010. A long-term laboratory test on staining susceptibility of esthetic composite resin materials. Quintessence international 41, 695-702.

Arun, D., Adikari Mudiyanselage, D., Gulam Mohamed, R., Liddell, M., Monsur Hassan,

N.M., Sharma, D., 2020. Does the Addition of Zinc Oxide Nanoparticles Improve the Antibacterial Properties of Direct Dental Composite Resins? A Systematic Review. Materials 14.
Aydin Sevinc, B., Hanley, L., 2010. Antibacterial activity of dental composites containing zinc oxide nanoparticles. Journal of biomedical materials research. Part B, Applied biomaterials 94, 22-31.
Bai, X., Lin, C., Wang, Y., Ma, J., Wang, X., Yao, X., Tang, B., 2020. Preparation of Zn doped mesoporous silica nanoparticles (Zn-MSNs) for the improvement of mechanical and antibacterial properties of dental resin composites. Dental Materials 36, 794-807.
Barbin, T., Velôso, D.V., Del Rio Silva, L., Borges, G.A., Presotto, A.G.C., Barão, V.A.R., Mesquita, M.F., 2020. 3D metal printing in dentistry: An in vitro biomechanical comparative study of two additive manufacturing technologies for full-arch implant-supported prostheses. Journal of the mechanical behavior of biomedical materials 108, 103821.
Cardoso, P.C., Espinosa, D.G., Mecenas, P., Flores-Mir, C., Normando, D., 2020. Pain level between clear aligners and fixed appliances: a systematic review. Progress in orthodontics 21, 3.
Chen, W., Qian, L., Qian, Y., Zhang, Z., Wen, X., 2021. Comparative study of three composite materials in bonding attachments for clear aligners. Orthodontics & craniofacial research 24, 520-527.
Eliades, T., Papageorgiou, S.N., Ireland, A.J., 2020. The use of attachments in aligner treatment: Analyzing the "innovation" of expanding the use of acid etching-mediated bonding of composites to enamel and its consequences. American journal of orthodontics and dentofacial orthopedics : official publication of the American Association of Orthodontists, its constituent societies, and the American Board of Orthodontics 158, 166-174.
Elshazly, T.M., Keilig, L., Salvatori, D., Chavanne, P., Aldesoki, M., Bourauel, C., 2022. Effect of trimming line design and edge extension of orthodontic aligners on force transmission: An in vitro study. Journal of dentistry 125, 104276.
Ersen, K.A., Gurbuz, O., Ozcan, M., 2020. Evaluation of polymerization shrinkage of bulk-fill resin composites using microcomputed tomography. Clinical oral investigations 24, 1687-1693.
Feinberg, K.B., Souccar, N.M., Kau, C.H., Oster, R.A., Lawson, N.C., 2016. Translucency, Stain Resistance, and Hardness of Composites Used for Invisalign Attachments. Journal of clinical orthodontics : JCO 50, 170-176.
Ferracane, J.L., 2006. Hygroscopic and hydrolytic effects in dental polymer networks. Dental materials : official publication of the Academy of Dental Materials 22, 211-222.
Garcia, I.M., Leitune, V.C., Kist, T.L., Takimi, A., Samuel, S.M., Collares, F.M., 2016. Quantum Dots as Nonagglomerated Nanofillers for Adhesive Resins. Journal of dental research 95, 1401-1407.
Garcia, I.M., Leitune, V.C.B., Visioli, F., Samuel, S.M.W., Collares, F.M., 2018. Influence of zinc oxide quantum dots in the antibacterial activity and cytotoxicity of an experimental adhesive resin. Journal of dentistry 73, 57-60.
Gulia, Rita Kakkar, S., 2013. ZnO Quantum Dots For Biomedical Applications. Advanced Materials Letters 4, 876-887.

He, H., Yang, D., Yuan, P., Shen, W., Frost, R.L., 2006. A novel organoclay with antibacterial activity prepared from montmorillonite and Chlorhexidini Acetas. Journal of colloid and interface science 297, 235-243.
Hollis, S., Eisenbeisz, E., Versluis, A., 2015. Color stability of denture resins after staining and exposure to cleansing agents. The Journal of prosthetic dentistry 114, 709-714.
Hu, H., Feng, C., Jiang, Z., Wang, L., Shrestha, S., Yan, J., Shu, Y., Ge, L., Lai, W., Hua, F., Long, H., 2020. Effectiveness of remineralizing agents in the prevention and reversal of orthodontically induced white spot lesions: a systematic review and network meta-analysis. Clinical oral investigations 24, 4153-4167.
Hua, F., Yan, J., Zhao, S., Yang, H., He, H., 2020. In vitro remineralization of enamel white spot lesions with a carrier-based amorphous calcium phosphate delivery system. Clinical oral investigations 24, 2079-2089.
Hua, F., Yang, H., He, H., 2018. Current Enamel Remineralization Therapies Have Limited Effects on Postorthodontic White Spot Lesions. The journal of evidence-based dental practice 18, 339-342.
Huang, M., Liu, S., Hua, F., 2022. Resin Infiltration May Be a Feasible Option to Esthetically Mask Enamel White Spot Lesions. The journal of evidence-based dental practice 22, 101715.
ISO, 2009. ISO 10993-5: 2009-Biological evaluation of medical devices-Part 5: Tests for in vitro cytotoxicity. International Standards Organization Geneva, Switzerland.
ISO, 2015. ISO/TS 11405: Dentistry–testing of adhesion to tooth structure. International Standards Organization Geneva, Switzerland.
ISO, 2019. ISO 4049-2019: Dentistry-Polymer-based Restorative Materials. International Standards Organization Geneva, Switzerland.
Jurubeba, J.E.P., Costa, A.R., Correr-Sobrinho, L., Tubel, C.A.M., Correr, A.B., Vedovello, S.A., Crepaldi, M.V., Vedovello, M.F., 2017. Influence of Thermal Cycles Number on Bond Strength of Metallic Brackets to Ceramic. Brazilian dental journal 28, 206-209.
Kim, B.R., Kang, S.M., Kim, G.M., Kim, B.I., 2016. Differences in the intensity of light-induced fluorescence emitted by resin composites. Photodiagnosis and photodynamic therapy 13, 114-119.
Lee, J., Choi, J.S., Yoon, M., 2014. Fabrication of ZnO nanoplates for visible light-induced imaging of living cells. Journal of materials chemistry. B 2, 2311-2317.
Liu, J., Zhang, H., Sun, H., Liu, Y., Liu, W., Su, B., Li, S., 2021. The Development of Filler Morphology in Dental Resin Composites: A Review, Materials.
Lopes, G.M., Prado, T.P., Camilotti, V., Bernardon, P., Mendonca, M.J., Ueda, J.K., 2021. In vitro and In vivo evaluation of resin composites fluorescence. Journal of the mechanical behavior of biomedical materials 114, 104223.
Low, B., Lee, W., Seneviratne, C.J., Samaranayake, L.P., Hagg, U., 2011. Ultrastructure and morphology of biofilms on thermoplastic orthodontic appliances in 'fast' and 'slow' plaque formers. European journal of orthodontics 33, 577-583.
Malekipour, M.R., Sharafi, A., Kazemi, S., Khazaei, S., Shirani, F., 2012. Comparison of color stability of a composite resin in different color media. Dental research journal 9, 441-446.
Mantovani, E., Castroflorio, E., Rossini, G., Garino, F., Cugliari, G., Deregibus, A.,

Castroflorio, T., 2019. Scanning electron microscopy analysis of aligner fitting on anchorage attachments. Journal of orofacial orthopedics = Fortschritte der Kieferorthopadie : Organ/official journal Deutsche Gesellschaft fur Kieferorthopadie 80, 79-87.
Moshiri, M., Eckhart, J.E., McShane, P., German, D.S., 2013. Consequences of poor oral hygiene during aligner therapy. Journal of clinical orthodontics : JCO 47, 494-498.
Mundim, F.M., Garcia Lda, F., Pires-de-Souza Fde, C., 2010. Effect of staining solutions and repolishing on color stability of direct composites. Journal of applied oral science : revista FOB 18, 249-254.
Rizk, S., 2022. Evaluation Methods of Depth of Cure and Polymerization Shrinkage for Dental Resin Composite Restorative Materials. Biomaterials Journal 1, 13-17.
Seneviratne, C.J., Leung, K.C., Wong, C.H., Lee, S.F., Li, X., Leung, P.C., Lau, C.B., Wat, E., Jin, L., 2014. Nanoparticle-encapsulated chlorhexidine against oral bacterial biofilms. PloS one 9, e103234.
Slot, D.E., Vaandrager, N.C., Van Loveren, C., Van Palenstein Helderman, W.H., Van der Weijden, G.A., 2011. The effect of chlorhexidine varnish on root caries: a systematic review. Caries research 45, 162-173.
Sun, J., Lin-Gibson, S., 2008. X-ray microcomputed tomography for measuring polymerization shrinkage of polymeric dental composites. Dental Materials 24, 228-234.
Talam, S., Karumuri, S.R., Gunnam, N., 2012. Synthesis, Characterization, and Spectroscopic Properties of ZnO Nanoparticles. International Scholarly Research Notices 2012, 1-6.
Tang, F., Li, L., Chen, D., 2012. Mesoporous silica nanoparticles: synthesis, biocompatibility and drug delivery. Advanced materials 24, 1504-1534.
Tavassoli Hojati, S., Alaghemand, H., Hamze, F., Ahmadian Babaki, F., Rajab-Nia, R., Rezvani, M.B., Kaviani, M., Atai, M., 2013. Antibacterial, physical and mechanical properties of flowable resin composites containing zinc oxide nanoparticles. Dental materials : official publication of the Academy of Dental Materials 29, 495-505.
Toledano, M., Osorio, R., Osorio, E., Fuentes, V., Prati, C., Garcia-Godoy, F., 2003. Sorption and solubility of resin-based restorative dental materials. Journal of dentistry 31, 43-50.
Tzankova, V., Aluani, D., Yordanov, Y., Valoti, M., Frosini, M., Spassova, I., Kovacheva, D., Tzankov, B., 2021. In vitro toxicity evaluation of lomefloxacin-loaded MCM-41 mesoporous silica nanoparticles. Drug and chemical toxicology 44, 238-249.
Vianna, J.S., Marquezan, M., Lau, T.C., Sant'Anna, E.F., 2016. Bonding brackets on white spot lesions pretreated by means of two methods. Dental press journal of orthodontics 21, 39-44.
Wang, H., Wang, S., Cheng, L., Jiang, Y., Melo, M.A.S., Weir, M.D., Oates, T.W., Zhou, X., Xu, H.H.K., 2019a. Novel dental composite with capability to suppress cariogenic species and promote non-cariogenic species in oral biofilms. Materials science & engineering. C, Materials for biological applications 94, 587-596.
Wang, N., Yu, J., Yan, J., Hua, F., 2023. Recent Advances in Antibacterial Coatings for Orthodontic Appliances. Frontiers in bioengineering and biotechnology 11, 99.
Wang, Q., Ma, J.B., Wang, B., Zhang, X., Yin, Y.L., Bai, H., 2019b. Alterations of the oral

microbiome in patients treated with the Invisalign system or with fixed appliances. American journal of orthodontics and dentofacial orthopedics : official publication of the American Association of Orthodontists, its constituent societies, and the American Board of Orthodontics 156, 633-640.
Wang, Y.-m., Li, J.-h., Hong, R.-y., 2012. Large scale synthesis of ZnO nanoparticles via homogeneous precipitation. Journal of Central South University 19, 863-868.
Winiarski, J., Tylus, W., Winiarska, K., Szczygieł, I., Szczygieł, B., 2018. XPS and FT-IR Characterization of Selected Synthetic Corrosion Products of Zinc Expected in Neutral Environment Containing Chloride Ions. Journal of Spectroscopy 2018.
Wu, Y., Yongtao, Y., Liu, H., Yao, X., Fan, L., Chen, Y., Tian, W., 2017. Long-term antibacterial protected cotton fabric coating by controlled release of chlorhexidine gluconate from halloysite nanotubes. RSC Advances 7, 18917-18925.
Xie, Y., Zhang, M., Zhang, W., Liu, X., Zheng, W., Jiang, X., 2020. Gold Nanoclusters-Coated Orthodontic Devices Can Inhibit the Formation of Streptococcus mutans Biofilm. ACS biomaterials science & engineering 6, 1239-1246.
Xu, B., Chen, X., Li, R., Wang, Y., Li, Q., 2014. Agreement of try-in pastes and the corresponding luting composites on the final color of ceramic veneers. Journal of prosthodontics : official journal of the American College of Prosthodontists 23, 308-312.
Yan, H., Wang, S., Han, L., Peng, W., Yi, L., Guo, R., Liu, S., Yang, H., Huang, C., 2018. Chlorhexidine-encapsulated mesoporous silica-modified dentin adhesive. Journal of dentistry 78, 83-90.
Yan, H., Yang, H., Li, K., Yu, J., Huang, C., 2017. Effects of Chlorhexidine-Encapsulated Mesoporous Silica Nanoparticles on the Anti-Biofilm and Mechanical Properties of Glass Ionomer Cement. Molecules 22.
Yan, J., Hua, F., Cao, L., Yang, H., He, H., 2022a. Multifunctional modification of orthodontic adhesives with ZnO quantum dots. Dental Materials.
Yan, J., Yang, H., Luo, T., Hua, F., He, H., 2022b. Application of Amorphous Calcium Phosphate Agents in the Prevention and Treatment of Enamel Demineralization. Frontiers in bioengineering and biotechnology 10, 853436.
Yang, H., Li, X., Xie, X., Wang, H., Ma, Y., Qiao, Q., Bai, Y., 2022. Yttrium aluminum garnet-based filler resin composites used as clear aligner attachments. Dental materials journal.
Yang, H.Y., Niu, L.N., Sun, J.L., Huang, X.Q., Pei, D.D., Huang, C., Tay, F.R., 2017. Biodegradable mesoporous delivery system for biomineralization precursors. International journal of nanomedicine 12, 839-854.
Zhang, J.F., Wu, R., Fan, Y., Liao, S., Wang, Y., Wen, Z.T., Xu, X., 2014. Antibacterial dental composites with chlorhexidine and mesoporous silica. Journal of dental research 93, 1283-1289.
Zhao, D., Song, H., Hao, L., Liu, X., Zhang, L., Lv, Y., 2013. Luminescent ZnO quantum dots for sensitive and selective detection of dopamine. Talanta 107, 133-139.

Table 1. Nitrogen adsorption desorption Results

Samples	S_{BET} (m^2/g)	V_p (cm^3/g)	D_p (nm)
pMSN	1694.8683	2.313997	4.6028
CHX@pMSN	597.1517	0.610608	3.9136

S_{BET}, specific surface area; V_p, average pore volume; D_p, average pore diameter; pMSN, pore-expanded mesoporous silica nanoparticles; CHX@pMSN: Chlorhexidine loaded pore-expanded mesoporous silica nanoparticles.

Table 2. Mean (standard deviation) of *CIE L*a*b** values of the resin discs from five groups.

	L*	a*	b*	ΔE
Control Group	76.03 (1.81) ^{ab}	1.64 (0.18) ^{a}	12.50 (0.65) ^{a}	1.60 (1.09) ^{a}
FAR	77.15 (1.72) ^{a}	1.99 (0.16) ^{b}	12.35 (0.73) ^{a}	1.99 (0.97) ^{a}
AFAR-1	76.72 (1.80) ^{a}	2.44 (0.19) ^{c}	13.07 (0.98) ^{a}	2.26 (0.74) ^{ab}
AFAR-2	75.95 (1.32) ^{ab}	2.67 (0.15) ^{d}	14.85 (0.58) ^{b}	2.90 (0.52) ^{b}
AFAR-3	74.85 (1.59) ^{b}	2.79 (0.19) ^{d}	17.22 (0.77) ^{c}	5.26 (0.74) ^{c}

FAR, fluorescent attachment resin; AFAR-1, antibacterial and fluorescent attachment resin-1; AFAR-2, antibacterial and fluorescent attachment resin-2; AFAR-3, antibacterial and fluorescent attachment resin-3. Non-identical letters (a, b, c, and d) indicate a statistically significant difference in each column (L*, a*, b*, and ΔE).

Table 3. Mean (standard deviation) of *ΔE* values after staining in tea, coffee and cola for 12 days.

ΔE	Control Group	FAR	AFAR-1	AFAR-2	AFAR-3
Tea	3.88 (0.94) ^{a}	4.19 (0.87) ^{a}	4.33 (1.13) ^{a}	4.79 (0.87) ^{a}	5.02 (1.14) ^{a}
Coffee	8.38 (0.60) ^{a}	8.42 (1.36) ^{a}	8.31 (1.23) ^{a}	8.90 (1.45) ^{a}	10.80 (1.98) ^{a}
Cola	4.03 (0.81) ^{a}	4.02 (0.57) ^{a}	3.24 (0.60) ^{ab}	2.95 (0.88) ^{ab}	2.32 (0.63) ^{b}

FAR, fluorescent attachment resin; AFAR-1, antibacterial and fluorescent attachment resin-1; AFAR-2, antibacterial and fluorescent attachment resin-2; AFAR-3, antibacterial and fluorescent attachment resin-3. Non-identical letters (a, b, c, and d) indicate a statistically significant difference in each row (tea, coffee, and cola).

Figure 1

Click here to access/download;Figure;Fig.1.tif

Fig. 1

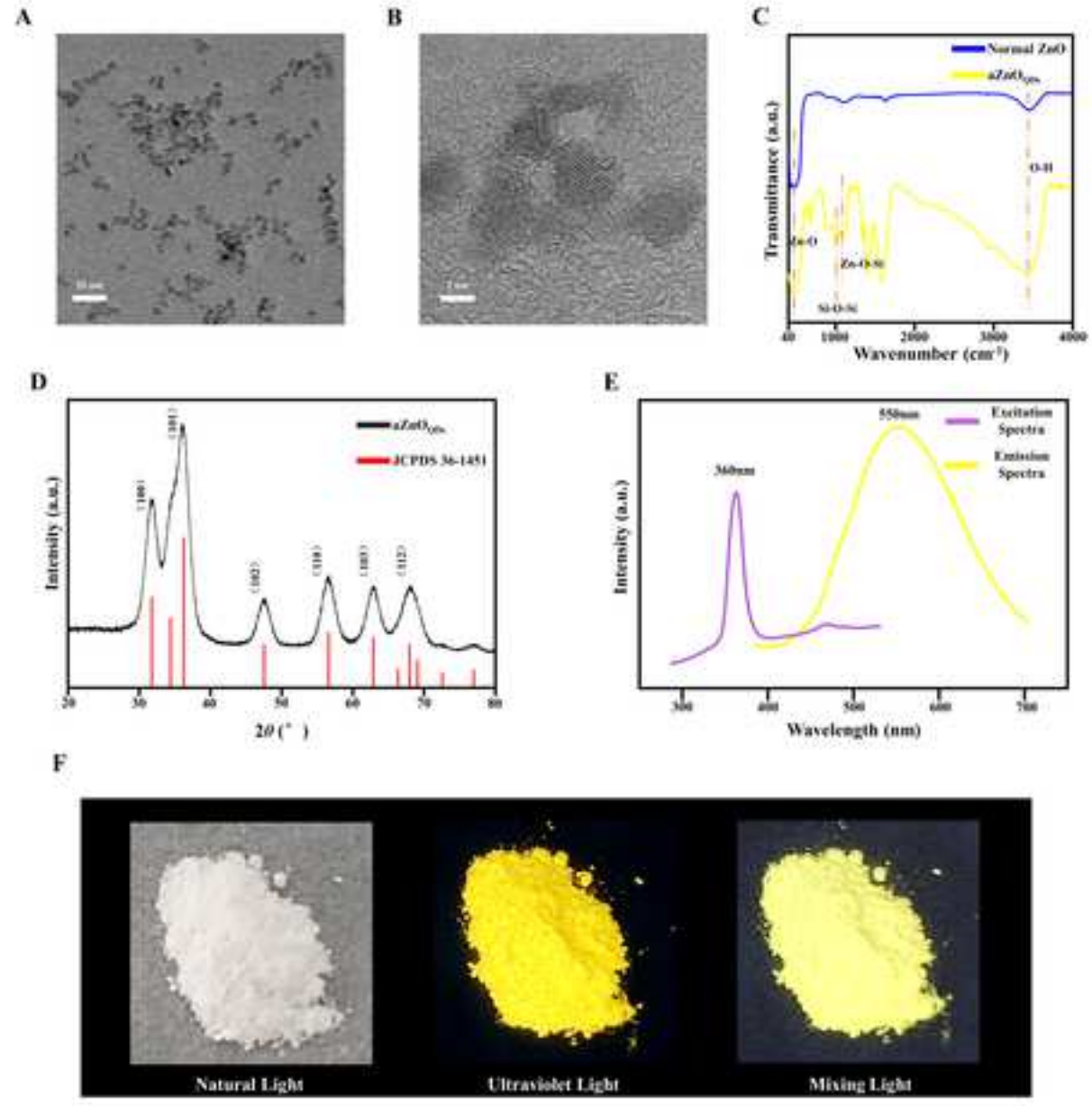

Figure 2

Click here to access/download;Figure;Fig.2.tif

Fig. 2

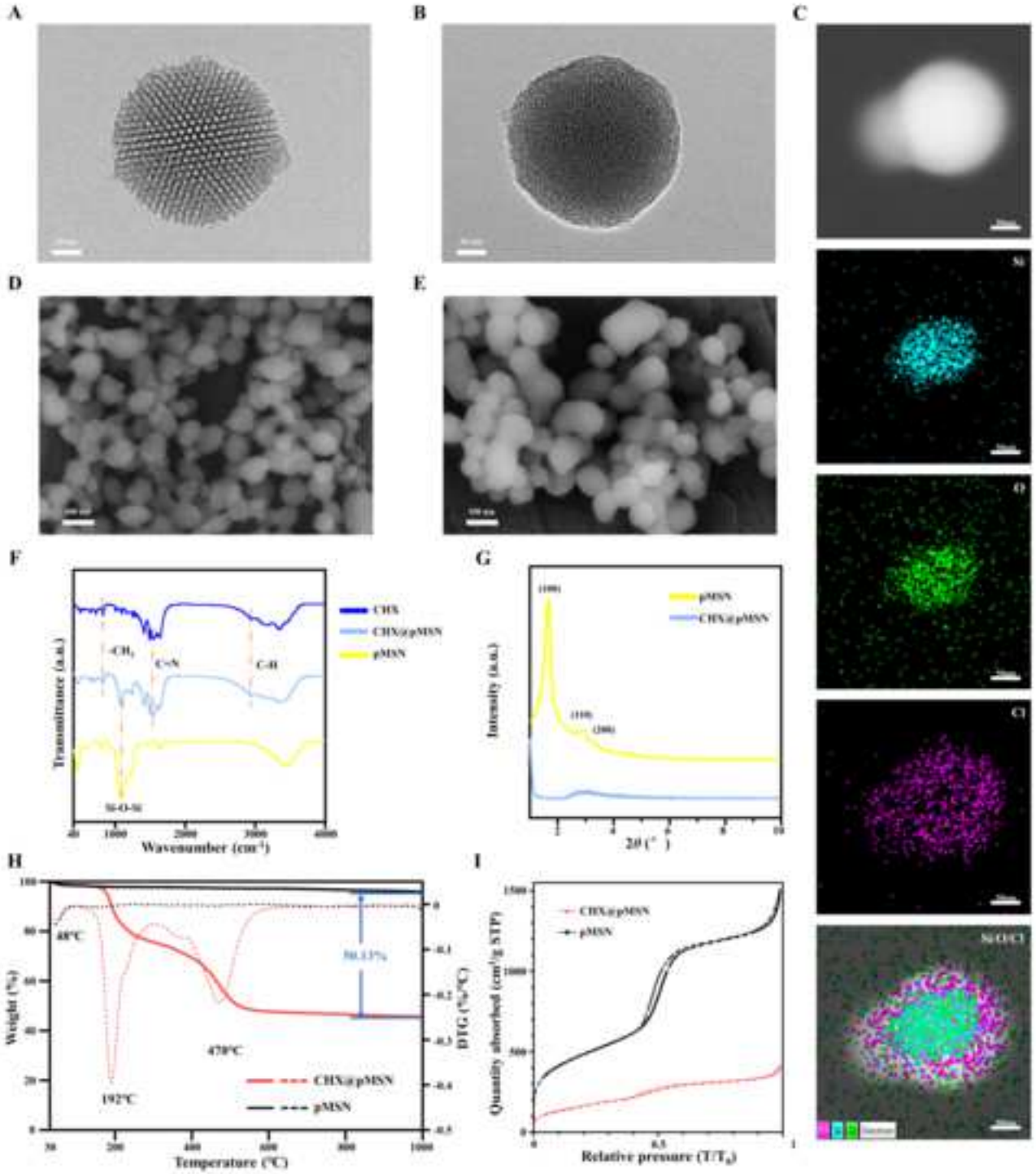

Fig. 3

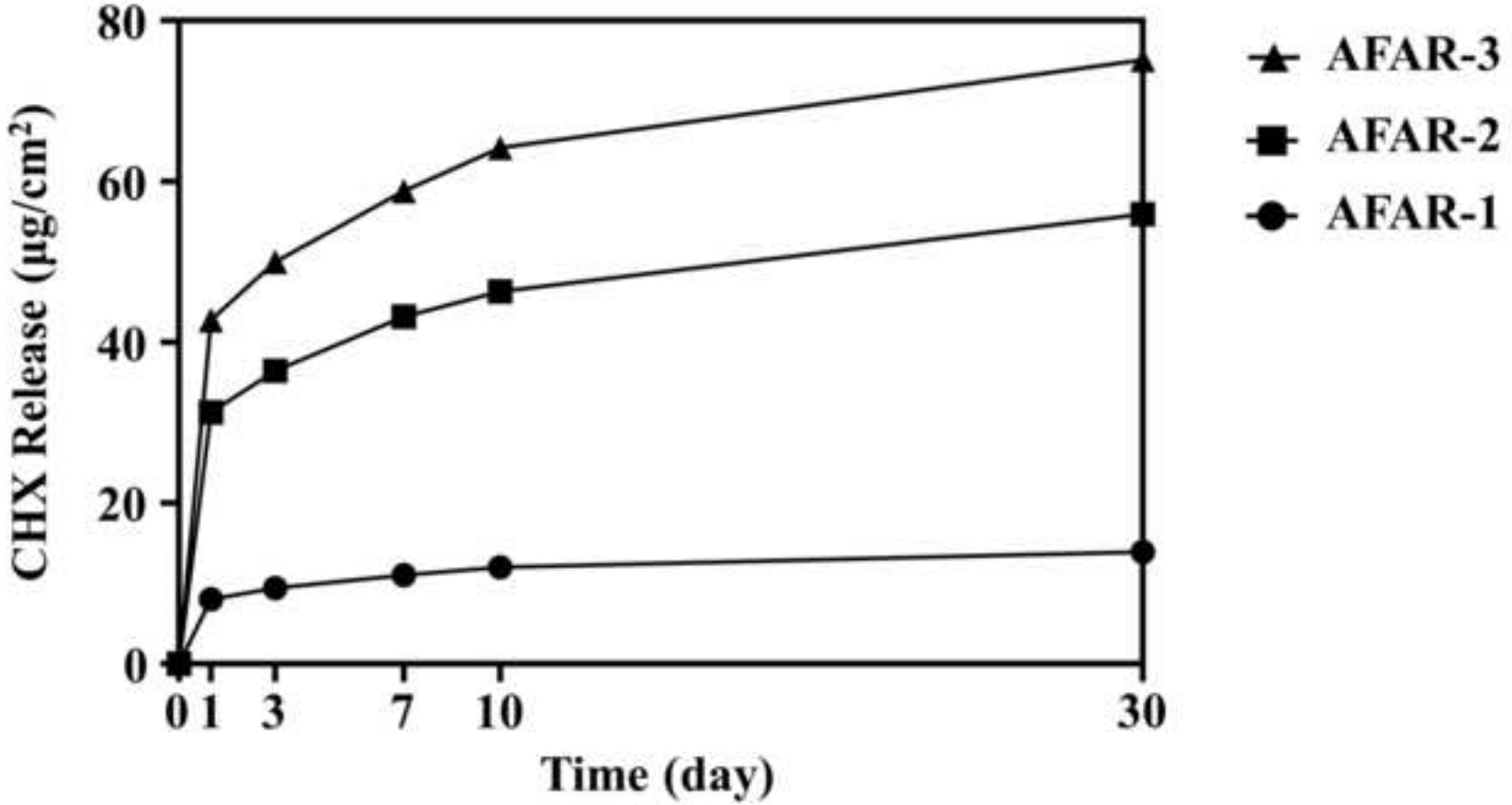

Fig. 4

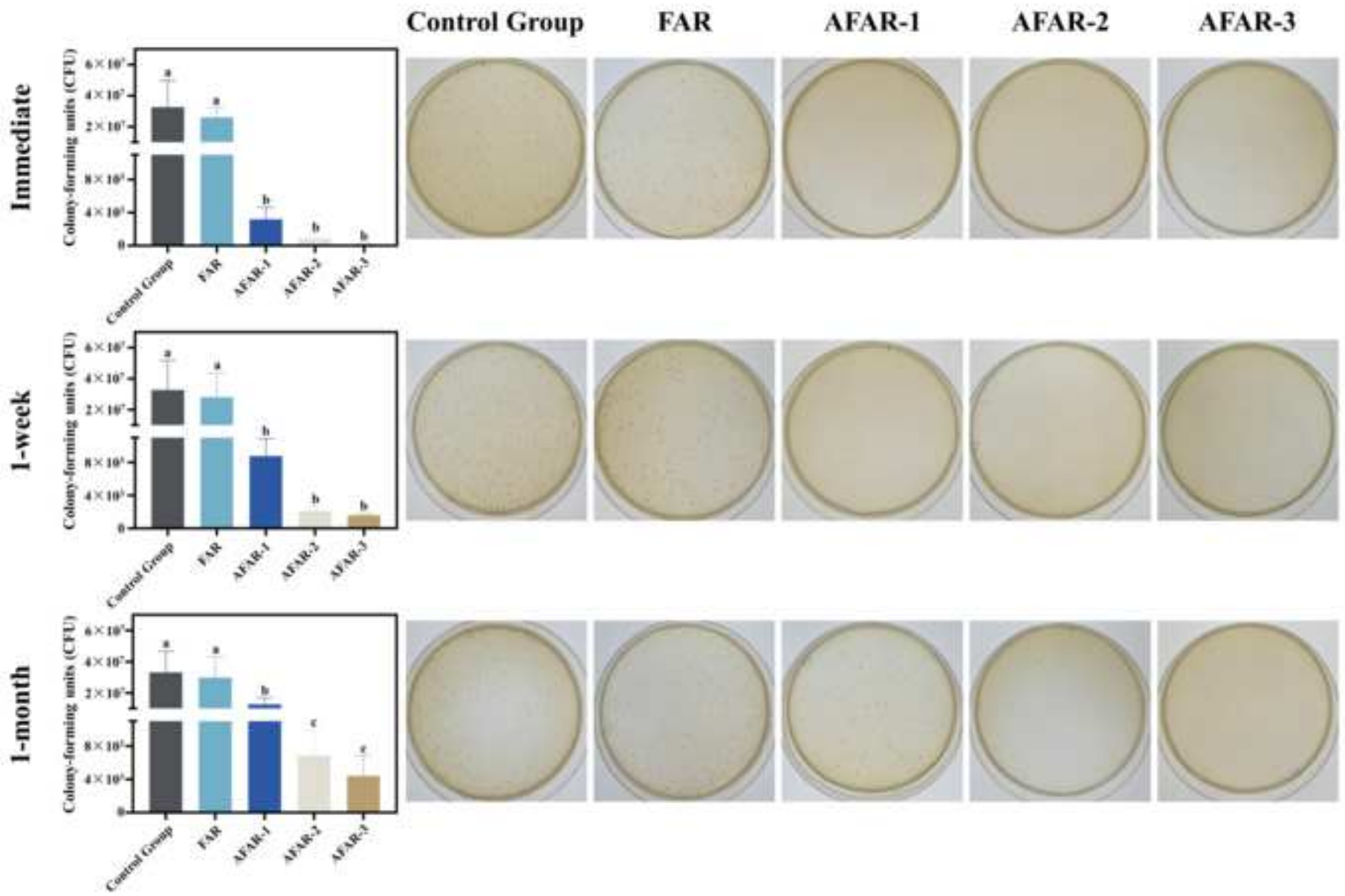

Fig. 5

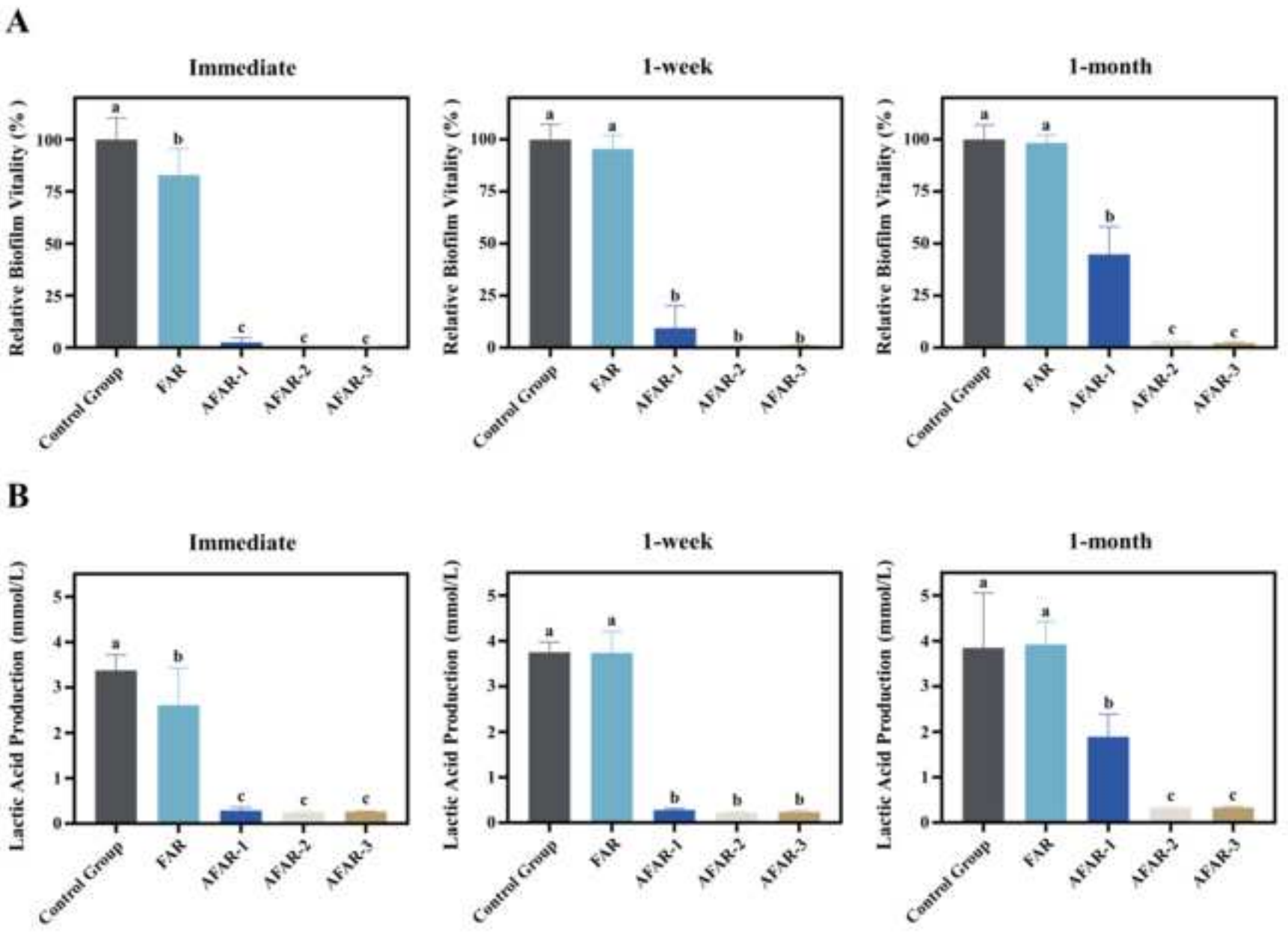

Figure 6

Click here to access/download;Figure;Fig.6.tif

Fig. 6

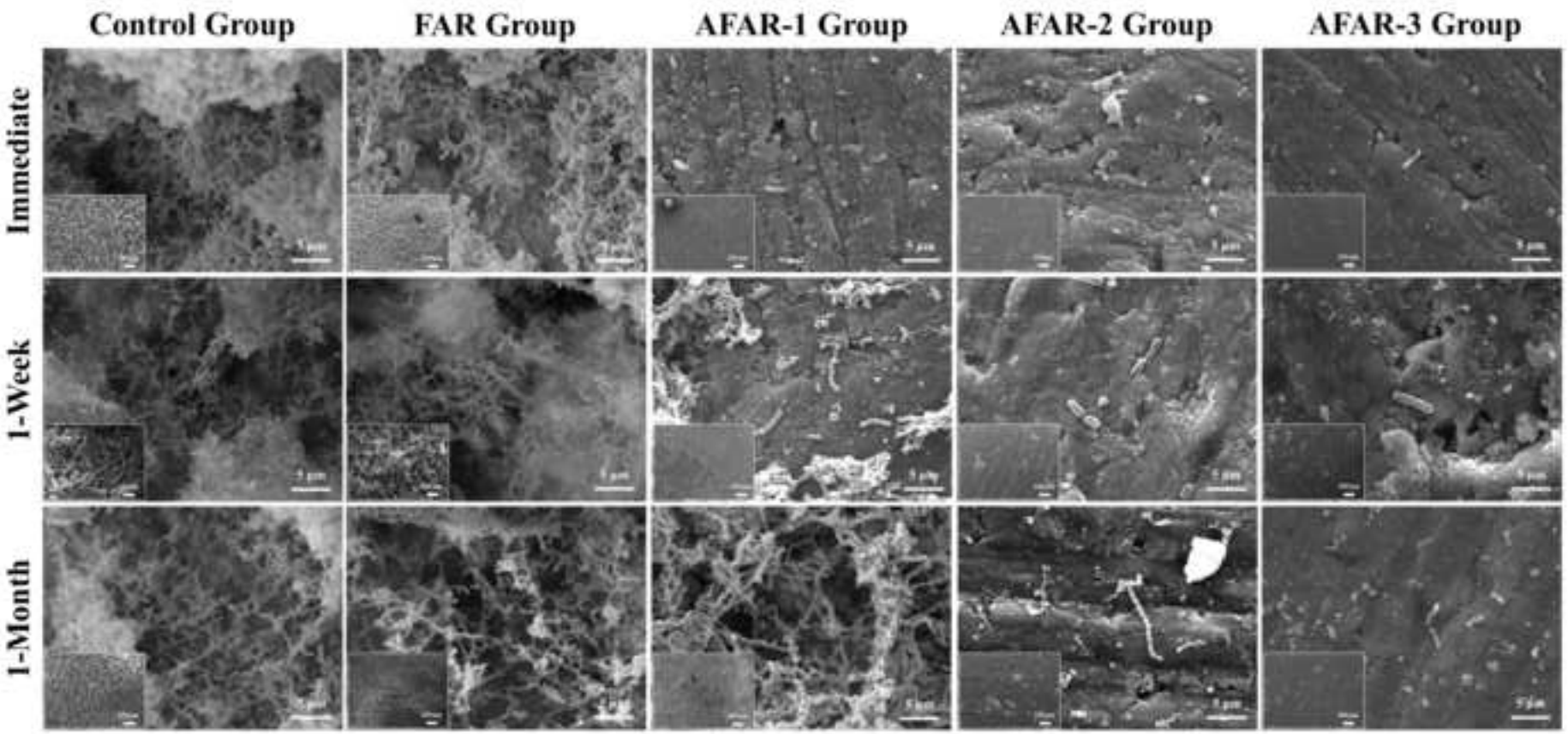

Fig. 7

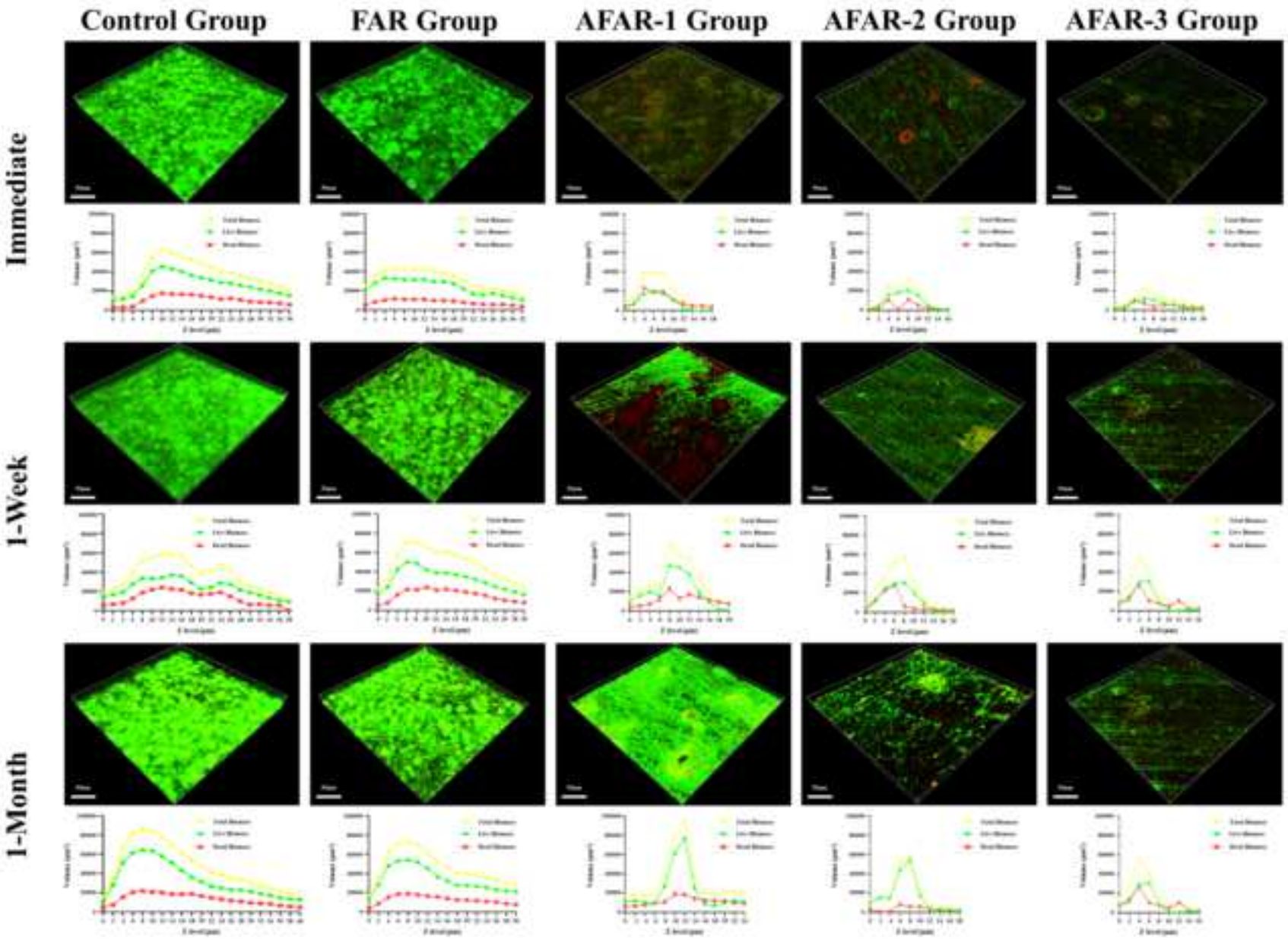

Fig. 8

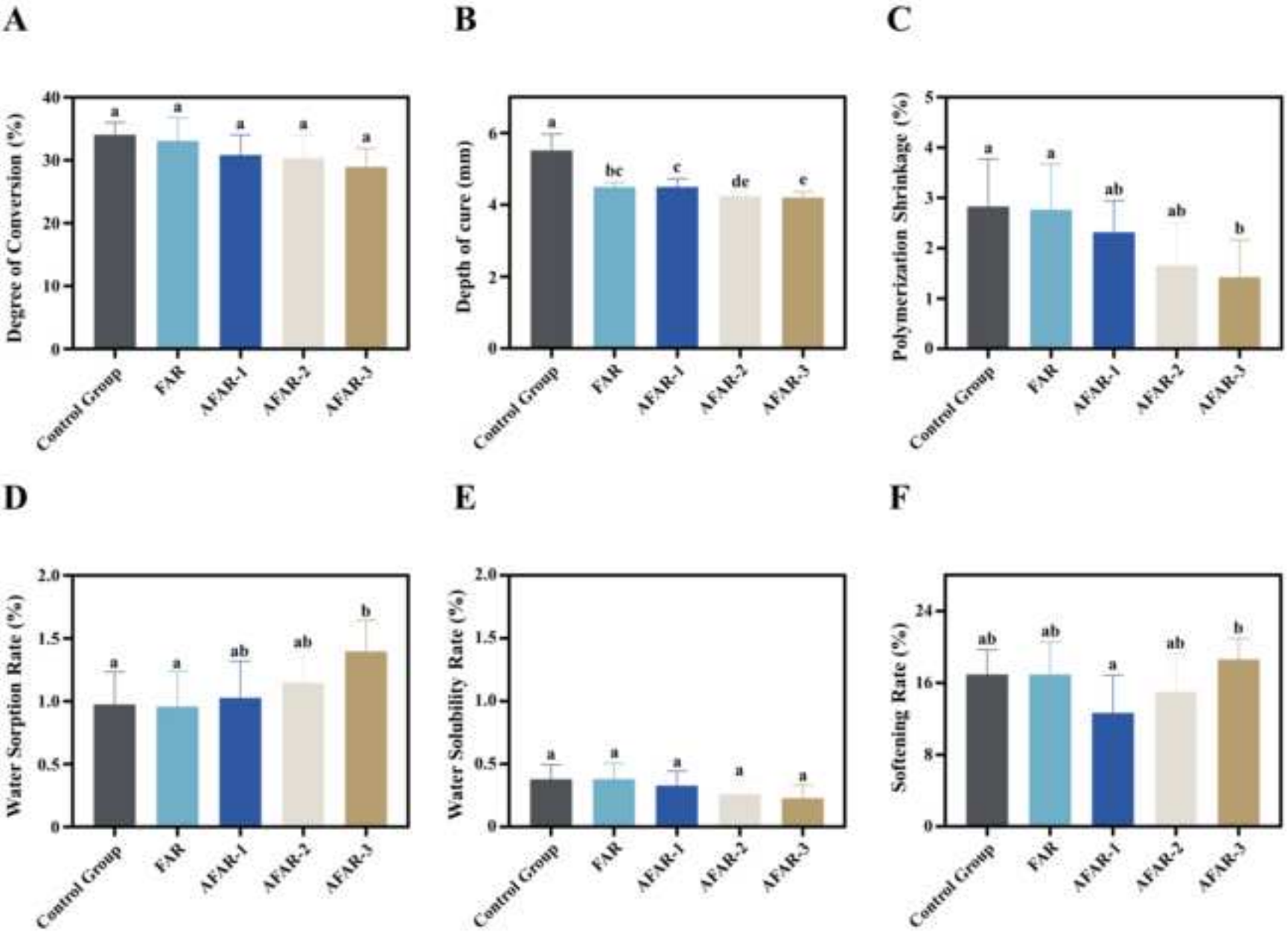

Fig. 9

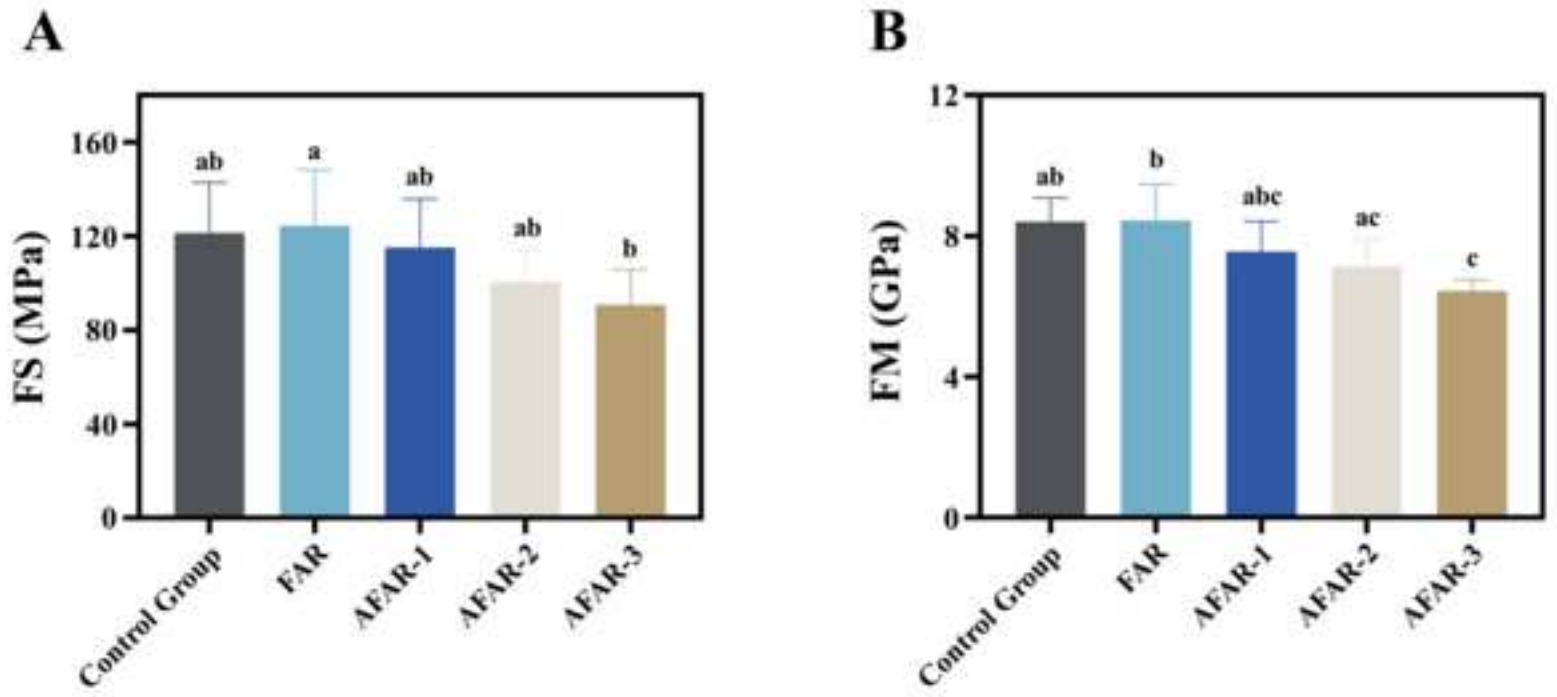

Fig. 10

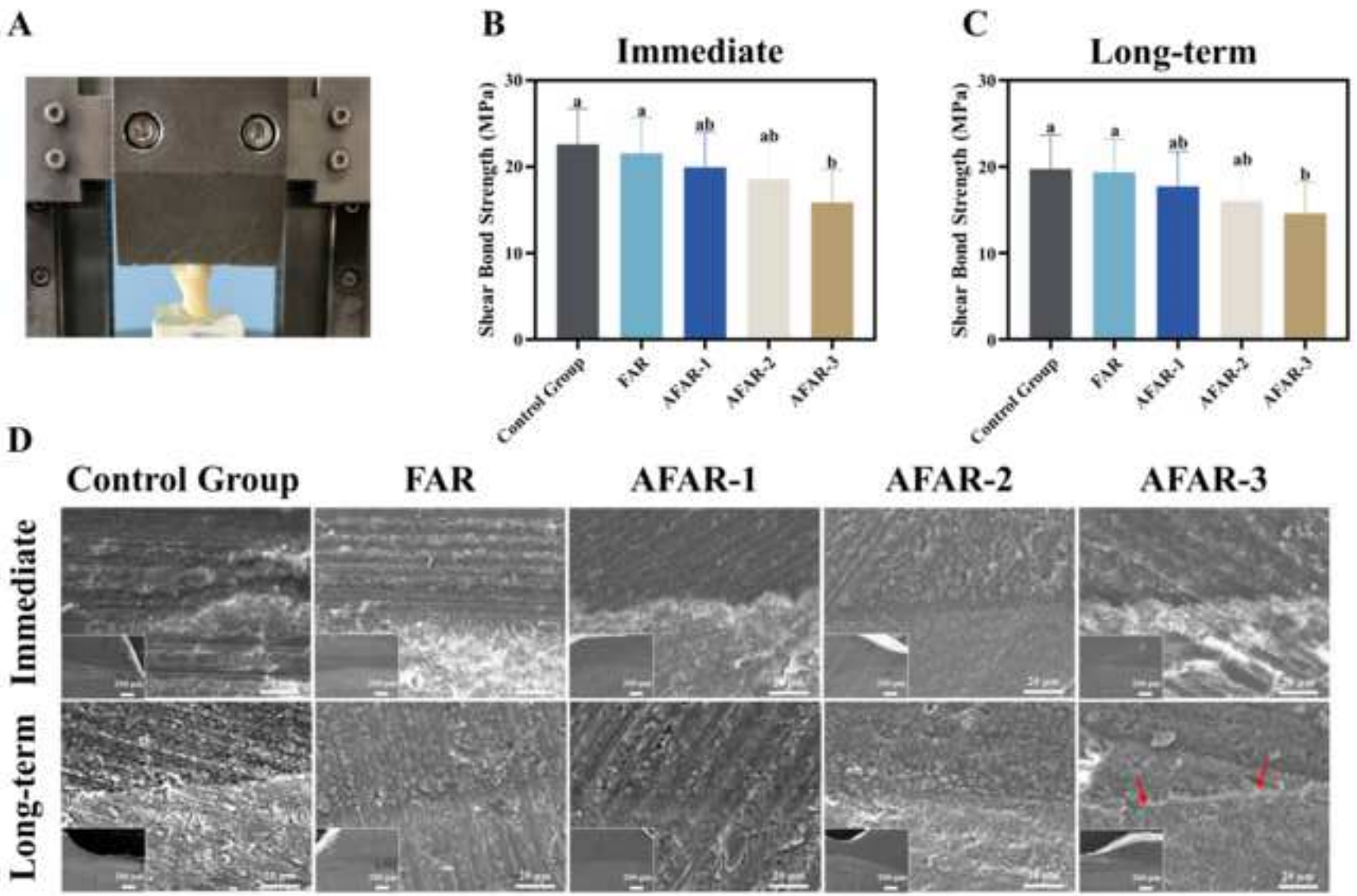

Fig. 11

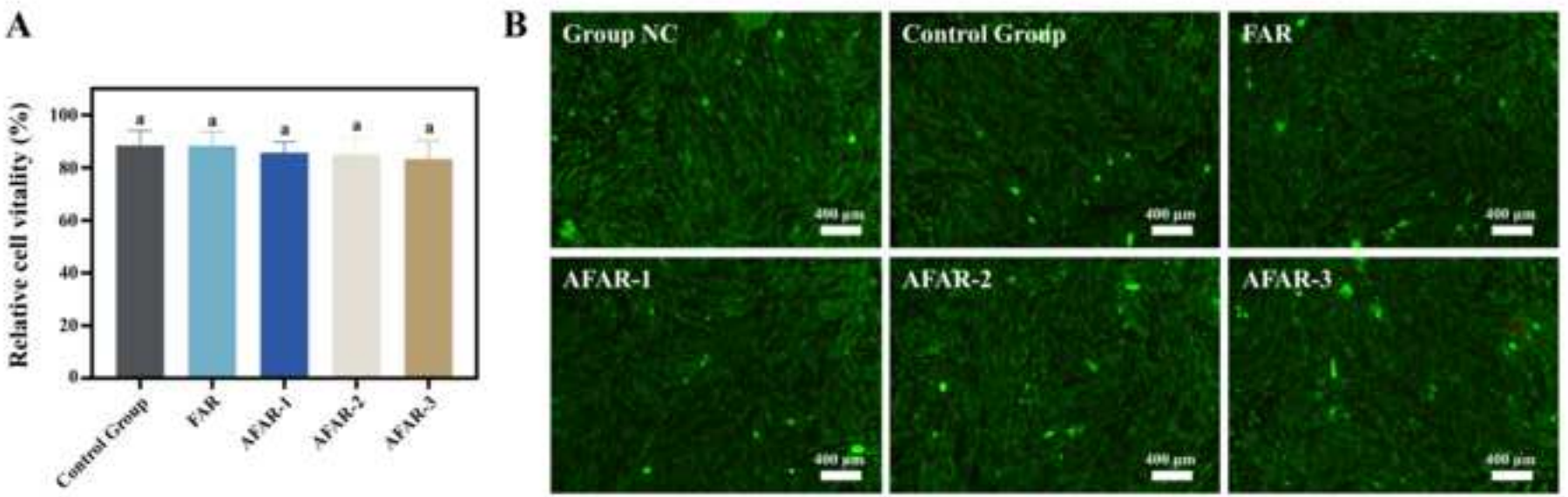

Fig. 12

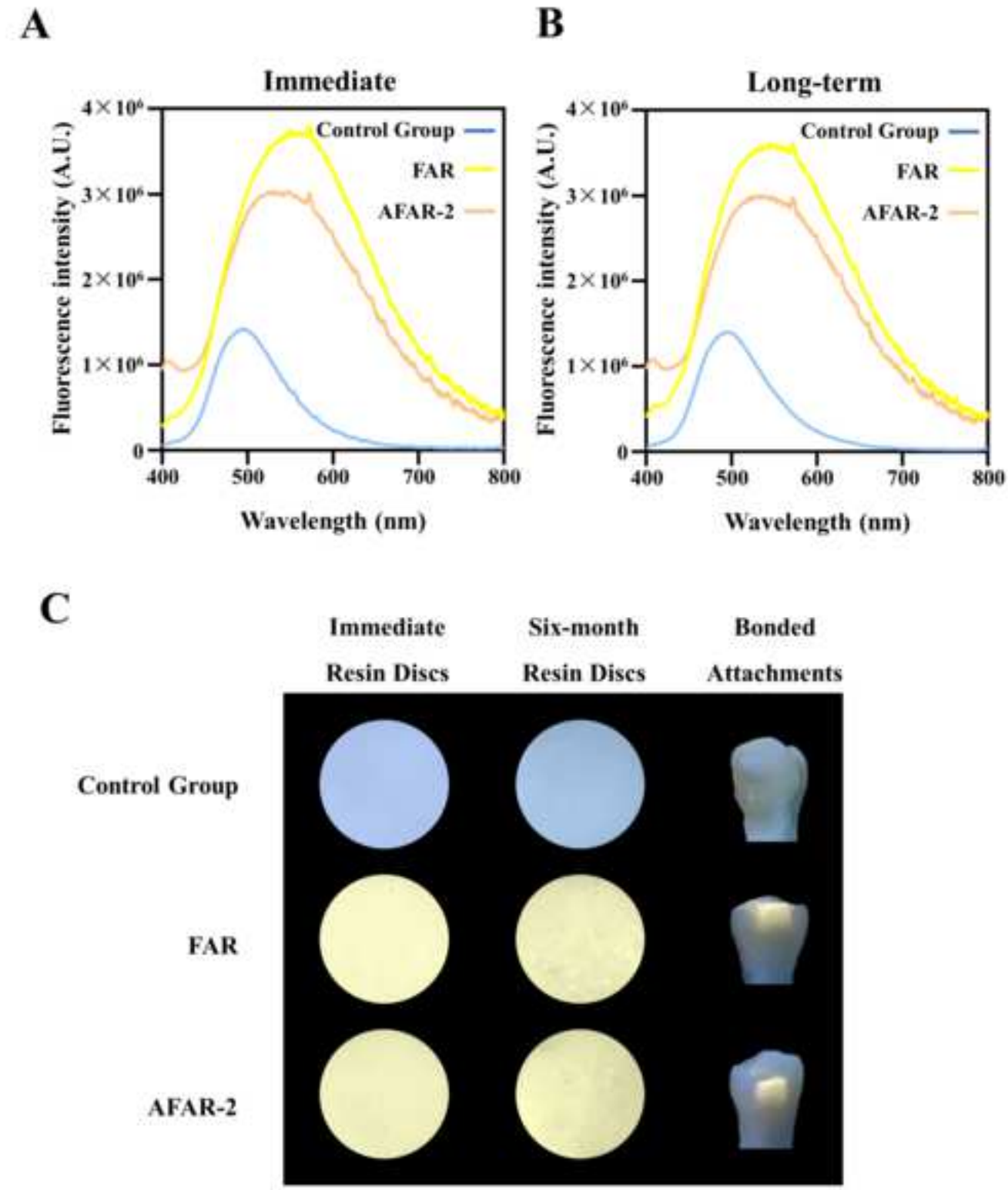

Figure Captions

Fig. 1. Characterization of $aZnO_{QDs}$. **(A).** TEM image at 100 kx magnification of $aZnO_{QDs}$. **(B).** TEM image at 800 kx magnification of $aZnO_{QDs}$. **(C).** FI-IR spectra of $aZnO_{QDs}$ and normal ZnO. **(D).** XRD pattern of $aZnO_{QDs}$. **(E).** Excitation and emission fluorescence spectra of $aZnO_{QDs}$. **(F).** Powder of $aZnO_{QDs}$ was white under natural light, ultraviolet light and mixing light (natural light mixing with ultraviolet light).

Fig. 2. Characterization of pMSN and CHX@pMSN. **(A).** TEM image of pMSN. **(B).** TEM image of CHX@pMSN. **(C).** Element mapping images of CHX@pMSN. **(D).** FESEM image of pMSN. **(E).** FESEM image of CHX@pMSN. **(F).** FI-IR spectra of CHX, CHX@pMSN and pMSN. **(G).** Small angle XRD of pMSN and CHX@pMSN. **(H).** Thermogravimetric analysis and differential thermal analysis of pMSN and CHX@pMSN. **(I).** Nitrogen adsorption-desorption ion analysis of pMSN and CHX@pMSN.

Fig. 3. Cumulative CHX releasing profile of AFAR-1. AFAR-2, and AFAR-3 groups at the time points of day 1, 3, 7, 10, and 30.

Fig. 4. CFU counting and representative images of bacterial colonies in the control, FAR, AFAR-1, AFAR-2, and AFAR-3 groups at the time points of immediate, 1-week aging, and 1-month aging. deviation. Data are shown as mean ± standard deviation. The groups labeled with the same letters have no significant difference ($P > 0.05$).

Fig. 5. (A). Relative biofilm viability of the control, FAR, AFAR-1, AFAR-2, and AFAR-3 groups at the time points of immediate, 1-week aging, and 1-month aging. **(B).** Biofilm lactic acid production of the control, FAR, AFAR-1, AFAR-2, and AFAR-3 groups at the time points of immediate, 1-week aging, and 1-month aging. Data are shown as mean ± standard deviation. The groups labeled with the same letters have no significant difference

($P > 0.05$).

Fig. 6. Biofilm SEM observation of the control, FAR, AFAR-1, AFAR-2, and AFAR-3 groups at the time points of immediate, 1-week aging, and 1-month aging. The magnification was 1 (upper) and 0.1 (lower left) kx.

Fig. 7. Biofilm 3D overlay CLSM images and corresponding distribution of live/dead bacteria biomass of the control, FAR, AFAR-1, AFAR-2, and AFAR-3 groups at the time points of immediate, 1-week aging, and 1-month aging.

Fig.8. Degree of conversion **(A)**, depth of cure **(B)**, polymerization shrinkage **(C)**, water sorption **(D)**, water solubility **(E)**, softening rate in solvent **(F)** of the control, FAR, AFAR-1, AFAR-2, and AFAR-3 groups. Data are shown as mean ± standard deviation. The groups labeled with the same letters have no significant difference ($P > 0.05$).

Fig.9. Flexure strength (FS) **(A)** and flexure modulus (FM) **(B)** of the control, FAR, AFAR-1, AFAR-2, and AFAR-3 groups. Data are shown as mean ± standard deviation. The groups labeled with the same letters have no significant difference ($P > 0.05$).

Fig.10. Shear bond strength (SBS) test and SEM observation of the bonding interfaces. **(A).** SBS test method. Immediate SBS **(B)** and long-term SBS **(C)** of the control, FAR, AFAR-1, AFAR-2, and AFAR-3 groups. Data are shown as mean ± standard deviation. The groups labeled with the same letters have no significant difference ($P > 0.05$). **(D).** SEM observation of the resin-enamel bonding interfaces of the control, FAR, AFAR-1, AFAR-2, and AFAR-3 groups immediately and after 5000 cycles of thermal cycling. The magnification was 1 (upper) and 0.1 (lower left) kx.

Fig.11. Biocompatibility evaluation. **(A)**. CCK-8 assay of the control group, FAR, AFAR-1, AFAR-2, and AFAR-3 groups. Data are shown as mean ± standard deviation. The groups labeled with the same letters have no significant difference ($P > 0.05$). **(B)**. Merged images

of Live/dead cell staining on HGFs of the group NC (natural culture group), control group, FAR, AFAR-1, AFAR-2, and AFAR-3 groups.

Fig. 12. (A). Immediate and long-term (six-month aging) fluorescence intensity of the control, FAR, and AFAR-2 groups. **(B).** Immediate and long-term (six-month aging) observation of resin discs and bonded clear aligner attachments of the control, FAR, and AFAR-2 groups under mixing light (natural light + ultraviolet light).